Preservation of mantle heterogeneities and serpentinization signature during antigorite dehydration: The example of the Bergell contact aureole

Romain Lafay, Lukas Baumgartner, Adélie Delacour

Received: 22 December 2021 | Revised: 14 August 2022 | Accepted: 3 September 2022

DOI: 10.1111/jmg.12699

ORIGINAL ARTICLE

Journal of METAMORPHIC GEOLOGY WILEY

Preservation of mantle heterogeneities and serpentinization signature during antigorite dehydration: The example of the Bergell contact aureole

Romain Lafay[1,2] | **Lukas P. Baumgartner**[2] | **Adélie Delacour**[3]

[1]Géosciences Montpellier, Université de Montpellier, Montpellier, France

[2]Institute of Earth Sciences, University of Lausanne, Lausanne, Switzerland

[3]UJM-Saint-Etienne, UCBL, ENSL, CNRS, LGL-TPE UMR5276, Univ Lyon, Saint Etienne, France

Correspondence
Romain Lafay, Géosciences Montpellier, Université de Montpellier, Place Eugène Bataillon, Montpellier, France.
Email: romain.lafay@yahoo.fr

Handling Editor: Dr. Katy Evans

Funding information
Schweizerischer Nationalfonds zur Förderung der Wissenschaftlichen Forschung, Grant/Award Numbers: 200020-172513, 200021-153094

Abstract

Major, minor, and trace element geochemistry as well as iron oxidation state and isotopes were investigated in serpentinites and olivine-talc fels present along a metamorphic gradient in the Bergell contact aureole (Central European Alps) to evaluate element mobility during serpentine. This aureole is an ideal target to study dehydration of mantle rocks due to the increase in temperature from greenschist facies conditions (350°C) to amphibolite facies conditions (750°C) at low pressures of 0.4 GPa. Petrography and geochemistry document several events of fluid–rock interaction and metamorphism. Serpentinization of the mantle rocks started on the ocean floor. Subsequent Alpine regional metamorphism led to the formation of antigorite-serpentinites containing olivine and diopside. These antigorite-serpentinites were transformed into olivine-talc fels in a large part of the contact-aureole. Bulk-rock major and trace element compositions maintain the geochemical signature of the precursor antigorite-serpentinites. No apparent changes are indeed observed despite the fact that major dehydration reactions occurred. In addition, changes neither in Fe^{3+}/Fe_{tot} ratio nor in $\delta^{56}Fe$ values were observed. Local composition variations of antigorite-serpentinites and olivine-talc fels reflect chemical heterogeneities related to protolith composition and serpentinization processes on the ocean floor prior to contact metamorphism. Hence, prograde dehydration reactions occurring during contact metamorphism did not induce substantial element mobility, change in redox state, or isotopic fractionation in these contact metamorphic rocks.

KEYWORDS
iron isotopes, olivine-talc fels, redox state, serpentinite breakdown, trace elements

1 | INTRODUCTION

The serpentine minerals are the main carriers of water in low to medium temperature mantle rocks (Ferrand, 2019, Ulmer & Trommsdorff, 1995). Serpentine dehydrates and releases volatiles to the overlying mantle wedge when heated during subduction (Deschamps et al., 2013; Marchesi et al., 2013; Scambelluri et al., 2019). Previous

studies have shown that, even before serpentine minerals react out of the rock, phase transition from lizardite, or chrysotile, to antigorite is associated with the release of fluid compatible elements (Li, B, Sr, Sb or Cs, e.g., Lafay et al., 2013; Vils et al., 2011). At higher metamorphic grades, the breakdown of antigorite also produces fluids enriched in those fluid-compatible elements, as suggested by studies of the chemical composition of serpentinite rocks and metaperidotites, as well as fluid inclusion studies (Deschamps et al., 2013; Peters et al., 2017; Scambelluri et al., 2019). The behaviour of some elements during dehydration reactions is well established, but the redox effects of fluids escaping subduction zones still remains largely unknown; both reduced (e.g., Piccoli et al., 2019) and oxidized fluids (e.g., Debret & Sverjensky, 2017) can be produced depending on the environment and the serpentinites oxidation degree (Evans & Frost, 2020; Frost & Beard, 2007). The large fluid discharge during serpentinite breakdown in convergent systems may account for intense metasomatism in the nearby units, and is one of the drivers of mantle wedge weakening (Reynard, 2013; Rutter & Brodie, 1988) and is responsible for important rheological changes within mantle units (Dilissen et al., 2018; Ganzhorn et al., 2019; Hirth & Guillot, 2013; Reynard, 2013).

Much progress has been made in recognizing initial oceanic crust geochemistry and geometry even after such rocks are deformed during subduction and exhumation of ophiolitic units. Good examples are the recently described Aiguilles Rouges oceanic core complex in the Western Alps (Decrausaz et al., 2021) and the ultramafites from Erro Tobbio (Scambelluri et al., 2001). Nevertheless, these relict structures do not provide the possibility to study a continuous metamorphic profile in a serpentinite unit, in contrast to contact metamorphic environments, in which serpentinites can be followed up-grade along a short distance to olivine-fels, as it is the case in the Bergell area (Central European Alps; Trommsdorff & Evans, 1972).

In the Bergell area, the high-temperature metamorphic gradient leads to the dehydration of the antigorite + olivine + diopside schists in the host rocks of the aureole to olivine + anthophyllite fels at the contact over approximately a 2-km distance (Figure 1). This allows the investigation of the geochemical evolution of ultramafic rocks along a continuous metamorphic gradient from greenschist facies conditions (<400°C) to amphibolite facies conditions (~750°C) at constant pressures of ~0.4 GPa. Here, antigorite breaks down to talc + olivine at a temperature of about 550°C producing a large amount of water. The talc + olivine paragenesis remains stable up to a temperature of approximately 680°C (Bromiley & Pawley, 2003; Chernosky et al., 1985; Evans, 1977; Trommsdorff & Evans, 1972). A drawback of this geodynamic setting is that extrapolation of the current results to subduction zone environments is complicated due to the fact that mass transport depends on infiltrating fluid volumes, fluid flow geometry and element solubility strongly depend on the pressure, not only on the temperature (e.g., Dolejš & Manning, 2010; Eugster & Baumgartner, 1987).

In this paper, we present bulk rock major and trace elements concentrations, Fe^{2+}/Fe^{3+} ratios and Fe isotope compositions of rocks from the Bergell contact aureole. Based on these geochemical data, we discuss element mobility, changes in iron oxidation state and iron isotope compositions during serpentine breakdown.

2 | GEOLOGIC SETTING

The Malenco unit is an ophiolite nappe located in the Central Alps (Figure 1a). It separates the Penninic and Austroalpine nappe stacks. The nappe consists of serpentinized peridotites with minor amounts of gabbros, along with some fragments of granulite facies lower crustal rocks (Figure 1b,c; see also Müntener & Hermann, 2001). The Platta-Malenco unit has been interpreted as a former ocean-continent transition (OCT) from the ancient Adriatic hyperextended margin (Müntener & Hermann, 2001). The nappe underwent greenschist facies regional metamorphism (450°C, 0.4–0.7 GPa; Guntli & Liniger, 1989) during Alpine convergence, at about 65 Ma (Jäger, 1973; Picazo et al., 2019). Metamorphism resulted in the formation of antigorite, olivine, diopside, chlorite, and magnetite schists, with accessory phases like Ti-clinohumite and sulfides (Evans & Trommsdorff, 1974).

The Austro-alpine-Penninic nappe stack was intruded by the Tertiary Bergell intrusive suite 32–30 Ma ago (Samperton et al., 2015). The intrusion consists of a sheet-like 2- to 3.5-km-thick tonalite. In the south-eastern part, the contact is subvertical and dips 70° towards east. The ultramafic rocks on the eastern side of the pluton are affected by contact metamorphism over a distance of about 2 km. Layering, interpreted to be primary mantle layering, strikes at a high angle to the contact in many places (Müntener & Hermann, 1996) and remains visible in the contact-metamorphosed rocks (Figure 2a,b). The NE part of the aureole displays nearly vertical lithological layering oriented roughly to 120° (normal to the intrusive contact, see dominant lithological layering in Figure 1). The SE part of the aureole displays a subhorizontal lithological layering oriented 50° to 60° (Figure 2a). An incipient foliation is subparallel to the lithological layering between the tonalite and the Insubric Line (Figure 1c).

The intrusion depth of the tonalite is constrained by the presence of andalusite and garnet-cordierite-biotite

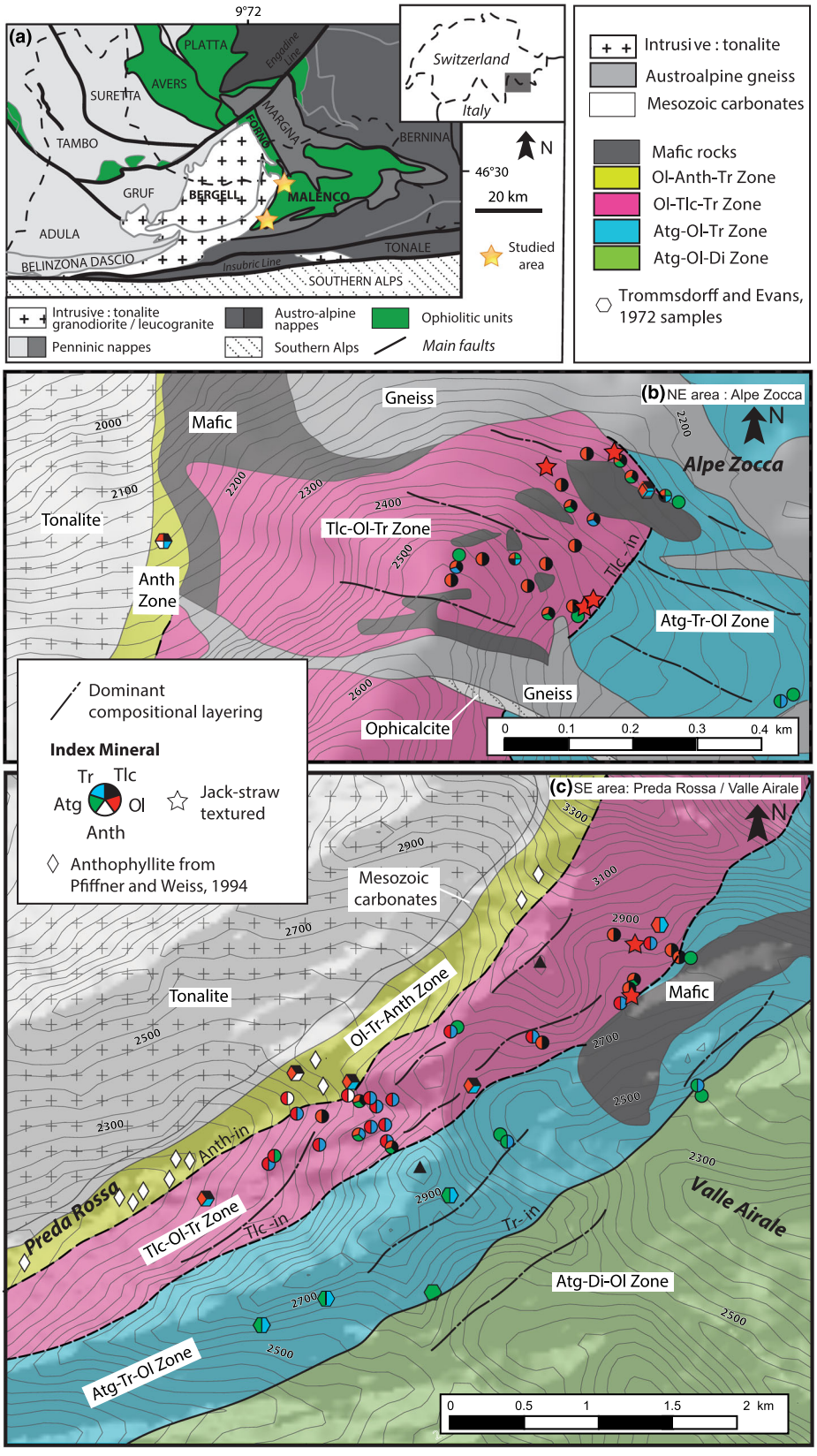

FIGURE 1 Tectonic maps of the Bergell intrusion area (a) and maps of the two contact-metamorphosed domains (b and c) investigated in the eastern side of the Bergell tonalite intrusion. Metamorphic zones are drawn on the basis of the detailed map from Montrasio et al. (2005) and our personal mineral assemblages identification. Samples from this study are reported as circle (the exact coordinates are provided in Table S1), with the typical paragenesis observed. Stars represent location where Jack-straw textures were observed. Hexagons represent the location of samples from Trommsdorff and Evans (1972) study and lozenges represent localities where anthophyllite has been recognized by Pfiffner and Weiss (1994). Anth: anthophyllite, Atg: antigorite, Ol: olivine, Tlc: talc, Tr: tremolite

assemblages consistent with a maximum pressure of 0.35 GPa (e.g., Wenk, 1973) for the north-eastern contact of the Bergell. By contrast, igneous hornblende barometry indicates a pressure of 0.45 to 0.65 GPa for the eastern Bergell margin (Davidson et al., 1996; Reusser, 1987). The contact metamorphism of the tonalite is well mapped and documented by several isograds. The following description is based on the classical work by

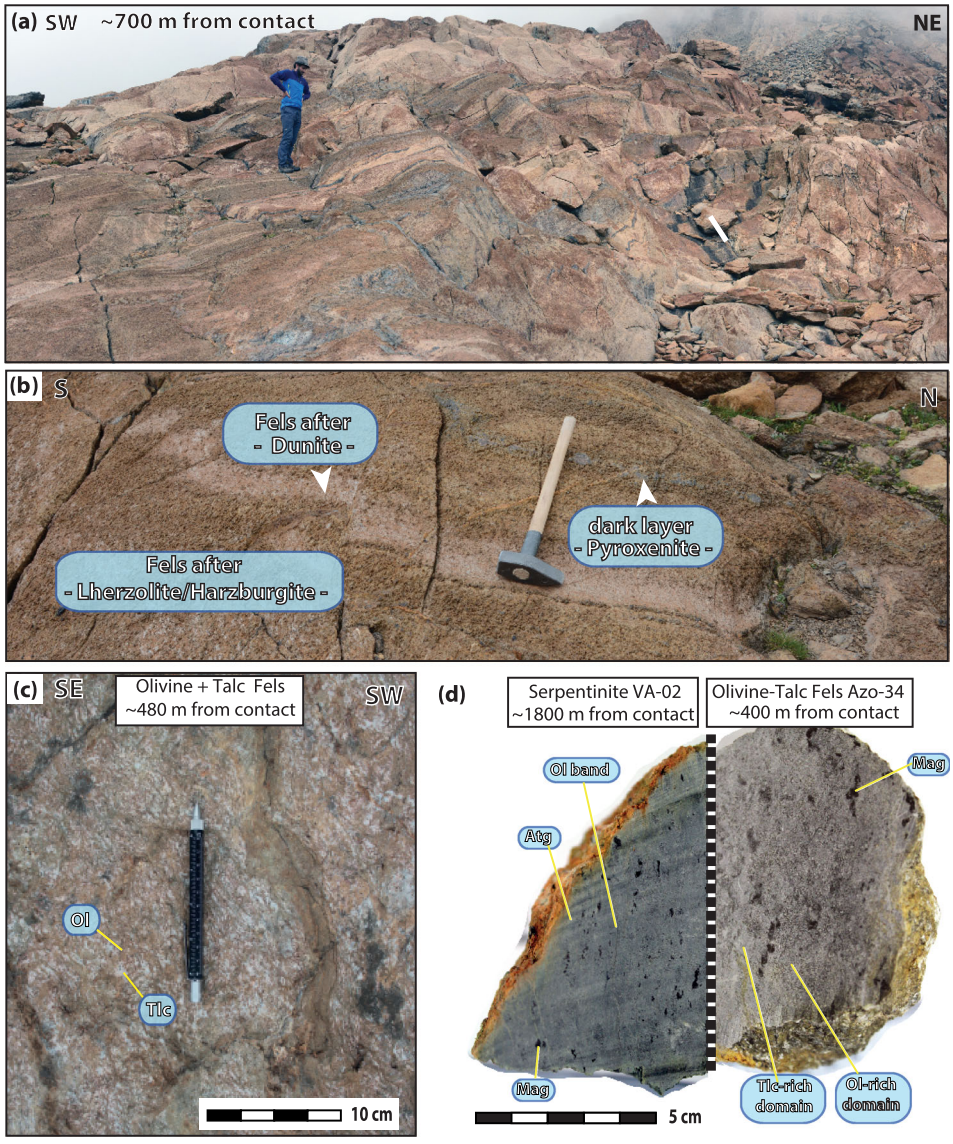

FIGURE 2 (a) Photographs showing preserved mantle layering in the southeastern part of the aureole and (b) close up view illustrating the layered aspect of the olivine-talc fels related to primary composition. (c) Photographs of olivine-talc fels. (d) Serpentinite and olivine-talc fels having comparable chemical composition found in the northeastern part of the aureole. Atg: antigorite, Ol: olivine, Mag: magnetite, Tr: tremolite, Tlc: talc

Trommsdorff and Evans (1972) and Trommsdorff and Connolly (1996). The major isograds are shown in Figure 1b,c. The first isograd is marked by the appearance of tremolite at the expense of diopside and antigorite, resulting in the paragenesis of olivine + serpentine + tremolite + chlorite + magnetite. At higher temperatures, antigorite breaks down to olivine and talc, resulting in a paragenesis of olivine + talc + tremolite + chlorite + magnetite. At the highest metamorphic grades, talc breaks down to anthophyllite (anthophyllite + olivine + tremolite + chlorite + magnetite). Locally, enstatite can be found at the contact due to anthophyllite breakdown. Modal abundances of individual phases can vary significantly, depending on the protolith (see discussion below). Samples collected for the present study were selected to minimize rare retrograde alteration after the contact metamorphism. Trommsdorff and Connolly (1996) estimated that the tremolite-in isograd occurred at 500°C (at 0.35 GPa), producing about 1.4 wt% water, and the antigorite breakdown to olivine and talc occurred at 530°C producing 4.4 wt% of water in their model composition.

The aureole is divided into two main domains: (1) The serpentinites and (2) the olivine-talc fels. The distinction between these two domains is marked by the appearance of talc and the disappearance of serpentine, that is, the talc-in isograd (Figure 1b,c). This isograd was drawn based on our observations (Figure 1c) and was extrapolated using the isograds from the Malenco geological map (Montrasio et al., 2005). Our observations are in good agreement with previous mapping and a recent detailed investigation of metamorphic veins in the N-E part of the aureole (Clément et al., 2019). Location and additional petrographic data are reported in the supporting information (Table S1).

3 | SAMPLING STRATEGY AND SAMPLE DESCRIPTION

Seventy-five samples, collected from 45 locations, were analysed for bulk rock chemical compositions. Three areas were targeted: the first one is Alpe Zocca, north-east of the tonalite (Figure 1b); the second and third areas are located south-east of the intrusion, at the uppermost part of the Valle Airale and the Valle di Preda-Rossa, respectively (Figure 1c). The samples were collected from both sides of the serpentine breakdown reaction to talc + olivine. In addition, the Val Airale area extends to within the anthophyllite zone.

We focused our investigations on diopside and/or tremolite-poor serpentinites and olivine-talc fels, though some of these samples contained up to 30 modal% by volume tremolite. The serpentinite breakdown isograd is readily mapped in the field. The tremolite-in and anthophyllite-in isograds are based on our samples, as well as the map of Clément et al. (2019) for the N-E area. Details of sample mineralogy, modal abundance of the major mineral phases, and coordinates of samples location are reported in the supporting information (Tables S1 and S2). Contact metamorphic minerals are easily recognizable (e.g., Figure 2c,d). Olivine formed during antigorite breakdown can be easily recognized around the isograd, where they form large and tabular crystals. Olivine produced at the tremolite isograd is however difficult to spot in the field and in thin section, because little minerals are formed, and olivine is already present from brucite breakdown inferred to have happened during the regional metamorphism (Trommsdorff & Connolly, 1996). Chlorite is stable in all rocks collected and is the only major aluminium-rich phase.

4 | ANALYTICAL METHODS

4.1 | Mineralogy identification

Polished thin sections were examined by optical microscopy using transmitted and reflected light to determine the microstructural features and the distribution of index minerals. The modal estimates of the index minerals are based on point counting and least-square fitting methods using mineral and bulk-rock compositions. They are reported in Table S2.

The mineralogy and composition of the index phases, magnetite, and sulfide for a selection of serpentinite and olivine-talc fels were verified using scanning electron microscope and microprobe analyses (see Tables S3, S4, S5, and S6).

4.2 | Raman spectroscopy

In situ Raman spectroscopy was used to identify serpentine phases in samples. Analyses were conducted at the Institut des Sciences de la Terre (University of Lausanne) using a Horiba HR Raman-FTIR spectrometer, consisting of an Olympus BX41 confocal microscope coupled to a 800-mm focal-length spectrograph. A 532.12-nm frequency-doubled Nd-YAG continuous-wave laser was focused on the sample with laser power at the sample surface of 19 mW. The Raman signal was collected in backscattered mode and calibrated with a silicon standard. The sampled volume was a few μm^3 using a 100× objective. Acquisition time for measurements was 5 × 30 s using a 1800 lines/mm grating. Spectra were recorded and interpreted using the software LabspecTM 4.14.

4.3 | Whole rock major elements measurements

Whole rock samples (cored or sampled with a hammer) were crushed using a tungsten mill to avoid contamination with additional SiO_2; contamination with tungsten, niobium, and tantalum might have occurred and hence these elements are not used in the discussion. Powdered samples were first dried at approximately 110°C. Loss on ignition (LOI) was determined by heating the sample to 1050°C for 2 h. Glasses were made by fusing 1.2 g of dried sample with 6 g of lithium tetraborate at 1300° for 3.5 min in a Pt-crucible. The disks were quenched into a homogeneous glass disk. Twenty serpentinites and 54 olivine-talc fels glasses were analysed by X-ray fluorescence using a Philips PW 2400 spectrometer at the ISTE laboratory (University of Lausanne). The international geostandards BR, UB-N, and PCC-1 were used as quality control. Uncertainties in XRF analyses are ±0.5 wt.% (2σ) for major components (SiO_2, MgO, Fe_2O_3, Al_2O_3, CaO) and ±0.01 wt% for minor elements (TiO_2, MnO, Na_2O, K_2O, Cr_2O_3, NiO).

The FeO content was quantified for 60 samples (18 serpentinites and 42 olivine-talc fels) by titration. About 200 mg of sample powder was dissolved in a solution of sulfuric and hydrofluoric acids and spiked with ammonium vanadate (NH_4VO_3) following the method of Wilson (1960). The solutions were analysed by colorimetry using a UV/Vis Perkin Elmer Lambda 25 spectrophotometer. The calibration curve used four standards with FeO compositions of 1.25 wt.% (NIM-L), 3.58 wt.% (SY-3), 5.17 wt.% (DR-N), and 8.63 wt.% (MRG-1) and a blank solution. The error on the standards were better than 3% relative. Duplicate analyses

on samples and standards give reproducibility better than 0.1 wt.%. Bulk analyses were corrected for the measured Fe^{2+}/Fe^{3+} ratios and analyses are reported in Table S3.

4.4 | Whole-rock trace elements measurements

Trace element abundances in samples were measured on pieces of Li-tetraborate glasses using a quadrupole spectrometer Agilent 7700 coupled to a GeoLas 200M ArF excimer ablation system at ISTE laboratory (University of Lausanne). NIST SRM612 was used as internal standard. The laser was operated with 10- to 20-Hz pulsing rate and a beam size of 90 μm. Prior to analysis, the clean glass surface was ablated with a short series of laser shots. The background was measured for 360 s to maximize sensitivity. Trace element concentrations were determined on the average of three repeated ablation intervals of 60 s and using bulk SiO_2 previously measured by XRF as an internal standard. Raw data were reduced off-line using the LAMTRACE software (Jackson, 2008). Results are reported in Table S3.

4.5 | Whole-rock iron isotopes measurements

Bulk Fe isotope compositions were measured on a selection of 21 samples (100-mg subsampling of crushed samples) and are presented in Table S3. Chemical separation of iron was performed in a clean room (Saint-Etienne) by anion exchange chromatography following the methods established by Busigny et al. (2014) and Dauphas et al. (2004) and slightly modified in order to totally dissolve Cr-spinel and magnetite. Iron isotope analyses were carried out on a MC-ICP-MS (Multi-Collector Mass Spectrometer) Neptune Plus at LMV Clermont-Ferrand. Simultaneous analyses of masses 54, 56, 57, 58 were performed and interferences of ^{54}Cr and ^{58}Ni were corrected through the measurements of ^{53}Cr and ^{60}Ni. Fe isotopes were measured on a high-resolution mode. Sample solutions were directly introduced into the plasma torch using a nebulizer introduction system. The combination of the nebulizer and the high-resolution mode allows interferences to be resolved while maintaining a stable signal throughout the entire analysis session. Analysed samples follow the mass fractionation line confirming that no interference on Fe masses occurred during the measurements. Instrumental mass bias was corrected using the standard bracketing method (Dauphas et al., 2009). The $^{56}Fe/^{54}Fe$ and $^{57}Fe/^{54}Fe$ ratios are expressed using the conventional δ notation in per mil (‰) deviation relative to IRMM-524 reference material (Craddock & Dauphas, 2011). Iron isotope composition of two international geo-standards IF-G and BCR-2 were analysed during each sample run to test the accuracy of the method. Mean $\delta^{56}Fe$ values of IF-G and BCR-2 were 0.642 ± 0.053 (1σ, $n = 12$) and 0.084 ± 0.063 (1σ; $n = 11$) in agreement with published data in Busigny et al. (2014). The reproducibility on samples is assessed through the analyses of three to four replicates with $2\sigma < 0.05$‰.

5 | RESULTS

5.1 | Petrographic characteristics of serpentinites and olivine-talc fels

5.1.1 | Serpentinites

Here, we classify as serpentinite all rocks below the talc-isograd. They are dominantly composed of antigorite (>50% by volume; Figure 2d), with variable proportions of olivine, chlorite, magnetite, clinopyroxene, and tremolite. For estimates of the modal abundance of samples, see Table S2.

Serpentinites in the aureole are weakly foliated antigorite serpentinites (confirmed by RAMAN spectroscopy, see Supporting Information). Serpentines occur in two textures: (1) Antigorite forms a homogeneous matrix composed of tiny blades (< 200 μm in length) or (2) as millimetre-size minerals (Figure 3a,b). These two textures likely correspond to former mesh and bastite textures typically found in serpentinites (Wicks & Whittaker, 1977). Olivine is commonly found as round crystals of few tens to hundreds of micrometres. They form layers and networks within the antigorite matrix. Serpentinites, which are not or slightly affected by the aureole (over a 1-km distance of the contact) contain regional metamorphic diopside porphyroblasts (Trommsdorff & Evans, 1972) and have identical antigorite textures (Figure 3a) to the contact metamorphosed serpentinites. Tremolite is typically present as randomly oriented or radial aggregates of idiomorphic crystals, up to several millimetres in size, that grew during contact metamorphism. Magnetite is present either as submillimetric oriented and elongated aggregates underlying a discrete planar layering (Figure 2d) or as micrometric euhedral crystals disseminated within the antigorite matrix. Furthermore, magnetite may additionally form small rods reflecting pristine mesh textures. In some cases, sulfides (pentlandite only) were found associated

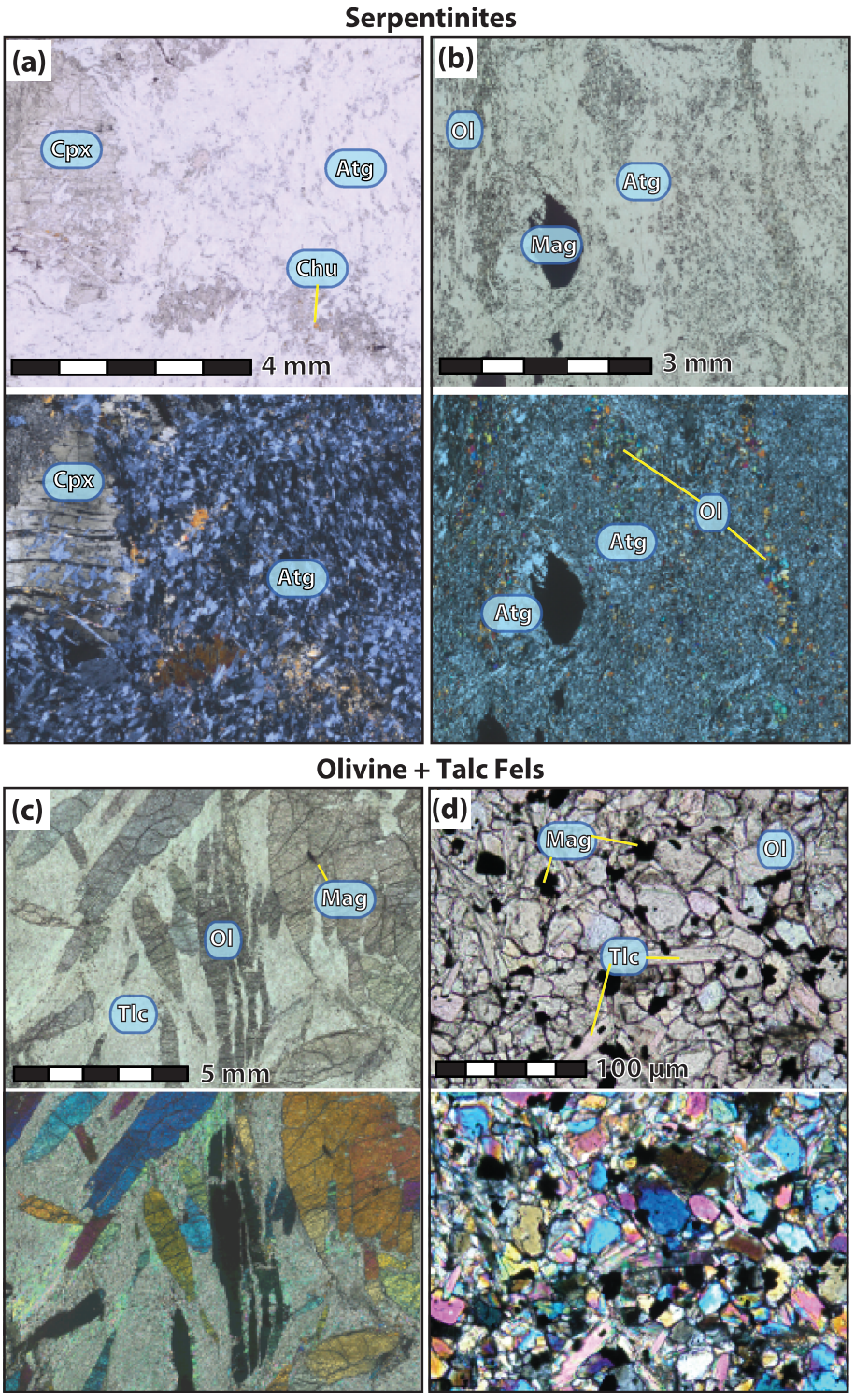

FIGURE 3 Thin-section photomicrographs of representative samples (top: normal light; bottom: cross polarized light). (a) Serpentinite from outside of the aureole (~3000 m from the contact E) containing rare clinopyroxene relics, (b) serpentinite with minor amount of metamorphic olivine (1800 m SE), (c) Jack-straw textured olivine-talc fels with centimetre-scale, planar olivine within a talc matrix (~750 m NE). (d) Olivine-talc fels with granoblastic olivine (<100 µm in size) with talc blades and isolated magnetite (~860 m SE). Atg: antigorite, Chu: Clinohumite, Cpx: clinopyroxene, Ol: olivine, Mag: magnetite, Serp: serpentine, Tlc: talc, Tr: tremolite

with the magnetite (see Supporting Information). Magnetite is present throughout the aureole. While grains seem to increase in size towards the intrusion it is not possible to establish clear cut reaction or recrystallization behaviour driving this.

No or very little retrograde alteration can be observed in these serpentinites. The microstructure are either prograde related to the regional metamorphic event during the upper Cretaceous (outermost aureole) or due to contact metamorphic recrystallization.

5.1.2 | Olivine-talc fels

Olivine-talc fels are easily recognizable in the field due to their bimodal red and white surface alteration

colour (Figure 2c). They are massive, in places with a layering marked by magnetite and/or chlorite bands reflecting the original layering. The talc-in isograd is surprisingly sharp and occurs over a few tens of meters in the field. Some partially reacted olivine-talc domains occur either as zones or as vein-like structures within the serpentinites close to the talc-in isograd (see also Clément et al., 2019). On the other side of the reaction isograd, some pods of relict massive serpentinites can be found inside the olivine-talc zone (see Lafay et al., 2019). Proportion of olivine, talc, and tremolite greatly varies within the olivine-talc fels (Table S2) reflecting variations in protolith and original bulk rock chemistry.

Contact metamorphic olivine occurs as prismatic, elongated subhedral porphyroblast up to a few centimetres in size close to the isograd (Lafay et al., 2019) or as a few hundreds of micrometre-sized polygonal or rounded crystals forming a granoblastic texture (Figure 3d) at higher metamorphic grade. These variations in size and textures reflect differences in reaction kinetics (Lafay et al., 2019). Olivine porphyroblasts contain numerous inclusions of antigorite, magnetite, chlorite, tremolite, and talc. In some localities—especially in the vicinity of the talc-in isograd—olivine has a plate-like shape with a high aspect ratio, up to 20:1, forming a Jack-straw texture (Figure 3c and Evans & Trommsdorff, 1974; Lafay et al., 2019). The large olivine crystals are either arranged in a criss-crossed pattern or are randomly oriented (Figure 3c). Talc forms fined-grained lepidoblastic flakes or is present as coarser crystal that does not exceed a few hundred micrometres (Figure 3c,d). The size of talc mineral is comparable with that of its antigorite precursor and magnetite is generally absent from the talc-rich aggregates.

Tremolite forms individual prismatic crystals or is present as acicular crystals in aggregates. Its proportion in the olivine-talc fels is commonly less than 10%, except for a few samples that were collected in the southeastern Preda-Rossa area (see Table S2 where it constitutes up to 31%). Magnetite is present as oriented submillimetric aggregates or as individual crystals of a few micrometres in size (Figure 2d and Supporting Information). Sporadically, pentlandite is associated with magnetite. Chlorite abundance increases in the olivine-talc fels relative to serpentinites (Table S2). Anthophyllite has been observed as fibrous crystals whose sizes are up to several hundred microns at Preda-Rossa and up to 250 m from the contact with the tonalite intrusion. In one sample from Preda Rossa (SE part of the aureole) at about 240 m from the contact, enstatite was observed as tiny tabular crystals intergrown with olivine (see Supporting Information).

5.2 | Geochemistry of serpentinites and olivine-talc fels

5.2.1 | Major element compositions

The bulk rock volatile content, expressed as loss on ignition (LOI), of serpentinites ranges between 7.5 and 12.95 wt%, while that of olivine-talc fels varies between 2.2 to 10.5 wt%. All oxide values were normalized to 100% on an anhydrous basis for representation into binary diagrams to avoid effects based on volatile content. Common characteristics to all samples are that their SiO_2 concentrations vary from 40.8 to 49.9 wt.%, while their concentrations in MgO vary between 36.4 and 47.5 wt.%. This corresponds to MgO/SiO_2 ratios of 0.80 to 1.15 (Table S3). Al_2O_3 content ranges between 0.27 and 4.38 wt.%, with $0.008 < Al_2O_3/SiO_2 < 0.1$ and CaO contents never exceed 4.9 wt.%. Approximately half of the samples collected have less than 0.5 wt.% CaO.

The compositions of most of the samples fall along a mantle partial melting trend, as seen in the CaO versus Al_2O_3 and MgO/SiO_2 versus Al_2O_3/SiO_2 diagrams (Figure 4). These two diagrams are typically used to illustrate fertile (Ca and Al-rich) to refractory (dunitic) mantle compositions. A few samples are depleted in CaO, while others are enriched. The seven Ca-rich olivine-talc fels samples are all from Alpe Zocca (Figure 4b). Based on the CaO versus Al_2O_3 diagram, we defined five groups of samples, each reflecting a protolith (Figure 4a,b): former dunite (A), Ca-poor harzburgite (B), harzburgite (C), Ca-rich harzburgite (D), and lherzolite (E). Lherzolites, harzburgites, and dunites define the mantle trend shown in Figure 4. A similar observation was made by Müntener et al. (2010), and the compositions of serpentinites outside the aureole, showing a regional metamorphism only, fully overlap the composition fields of serpentinites inside the aureole.

FeO_{Total} ($FeO + Fe_2O_3$) content varies from 3.94 to 10.21 wt.% in serpentinites and 7.08 to 13.27 wt.% in olivine-talc fels. The Mg-number (Mg#), taking into account only FeO, varies from 0.88 to 0.94 for all rocks where Fe^{2+} content was determined (average at 0.9). A group of 7 serpentinites, plotting in the upper Mg-value range ($0.93 < X_{Mg} < 0.95$; Figure 5a) and which seem to have escaped the talc-in reaction, was collected in serpentinite lenses found inside the talc-in isograd and is essentially composed of dunites and Ca-poor harzburgites.

5.2.2 | Iron redox state and iron isotope compositions

The bulk Fe^{3+}/Fe^{2+} ratio varies between 0.4 and 2.35 in serpentinites (Figure 5a) and between 0.15 and 3.36 in

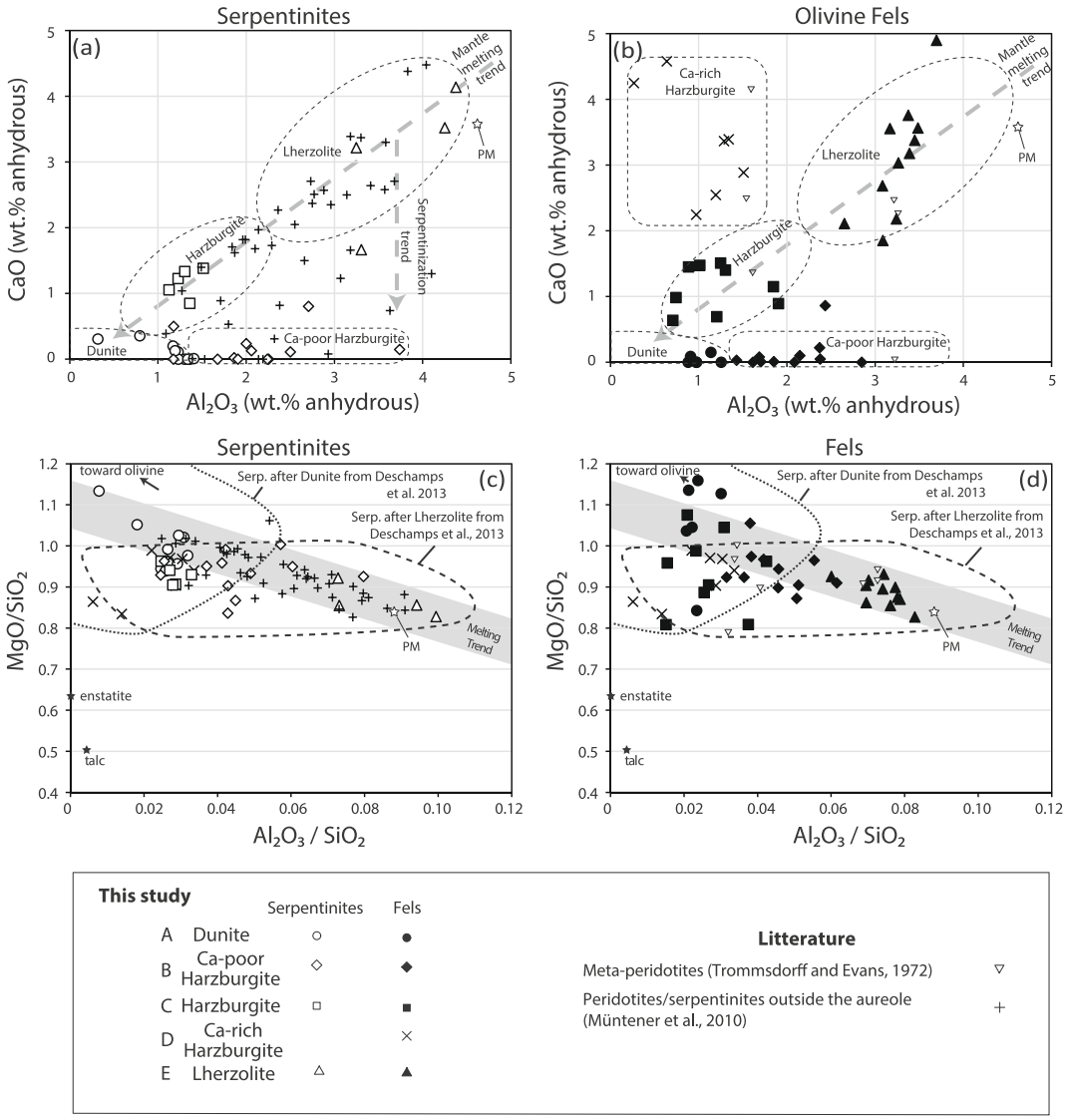

FIGURE 4 Binary elementary concentrations diagrams: (a,b) CaO versus Al_2O_3 for serpentinites and olivine fels respectively and (c,d) MgO/SiO_2 versus $Al2O_3/SiO_2$ diagrams for serpentinites and olivine fels, respectively. They illustrating the position of contact aureole rocks following the melting trend and the departure of this trend for rocks defined as Ca-poor and Ca-rich harzburgite. Compositions are recalculated on a volatile free basis. Symbol distinction was made on the basis of the assumed rock protolith defined from figure (a,b) with a distinction between dunite, harzburgite, Ca-poor and Ca-rich harzburgite as well as lherzolite. Data from the aureole after Trommsdorff and Evans (1972) and data from far-field serpentinite after Müntener et al. (2010) are also reported for comparison. The primitive mantle values (PM) are from McDonough and Sun (1995). In (c,d), the bulk silicate evolution trend so-called "terrestrial array" after Jagoutz et al. (1979) is reported and the typical fields for serpentinite after dunite and serpentinite after lherzolite are from Deschamps et al. (2013) (D). en: enstatite, ol: olivine, tlc: talc

olivine-talc fels (Figure 5b). The values cluster for both serpentinites and olivine-talc rocks between 0.5 and 1.5. Only 5 samples, classified as Ca-poor harzburgite or dunites, have a Fe^{3+}/Fe^{2+} ratio greater than 2 (Figure 5). While there is an inverse trend between Fe^{2+} and Fe^{3+} in Figure 5a,b, there is no correlation between Mg# and Fe^{3+}/Fe_{tot} nor is there a correlation of this ratio with LOI (Figure 5c) or CaO/Al_2O_3 ratios (Figure 5d). Generally, scatter in Fe^{3+}/Fe_{tot} ratios is larger in the less fertile rock types, dunites and Ca-poor harzburgites, than in lherzolite and harzburgite rock types (Figure 5c–e).

Bulk rock $\delta^{56}Fe$ values vary from −0.12 to +0.14 ‰ (Figure 6). Their values correspond to the range reported for other alpine serpentinites (Debret et al., 2016) and mantle peridotites (Beard et al., 2003; Craddock et al., 2013; Dauphas et al., 2009; Weyer & Ionov, 2007; Williams & Bizimis, 2014). A large scatter is observed when plotting $\delta^{56}Fe$ values against Fe^{3+}/Fe_{tot} ratios (Figure 6a). However, a slight positive correlation exists between $\delta^{56}Fe$ values and Fe^{3+}/Fe_{tot} ratios, except for two serpentinite samples (a meta-dunite and a meta-harzburgite). If the two samples are excluded, the

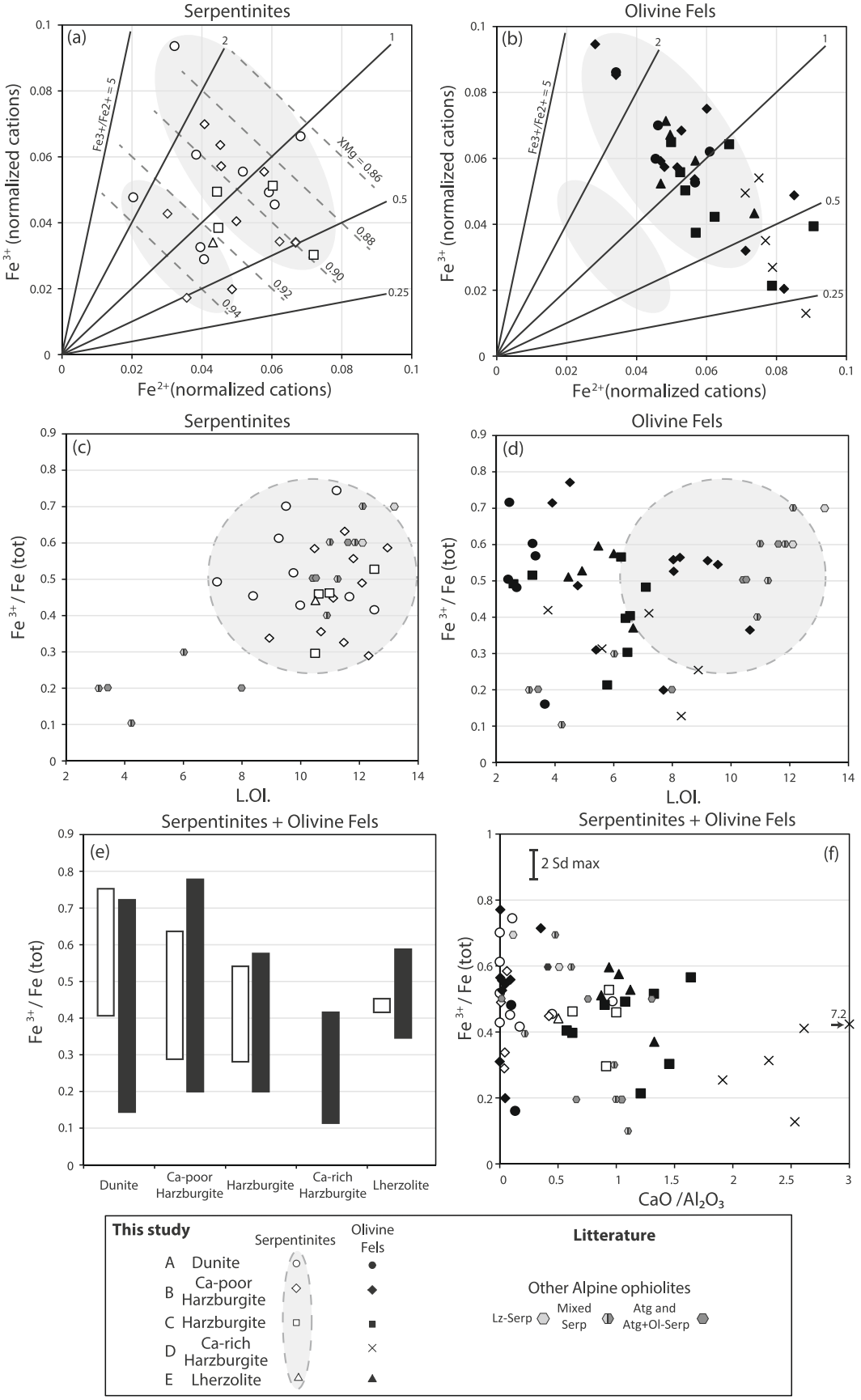

FIGURE 5 Legend on next page.

FIGURE 5 Binary diagrams showing: (a,b) Fe^{3+} versus Fe^{2+} (the dashed ellipse surrounds the Fe-poor serpentinites) for serpentinites and olivine fels respectively (c,d) Fe^{3+}/Fe_{tot} versus loss on ignition (LOI) for serpentinites and olivine fels respectively, (e) boxplot Fe^{3+}/Fetot for the different lithologies recognized in the field area, (f) Fe^{3+}/Fetot versus CaO/Al_2O_3. This illustrates the broad field of composition for contact aureole ultramafic rocks and the independence of both iron oxidation state and isotope composition with metamorphic imprint and the independence between this two parameters. Data for meta-serpentinites (Lz-Serp.: Lizardite serpentinites and Atg [Atg + Ol]-Serp.: Antigorite and antigorite + olivine serpentinites) from other alpine localities (Lanzo, Monte-Maggiore, and Montgenèvre ophiolite; Debret et al., 2013, 2014, 2016) are shown as a comparison in binary diagram (c to e).

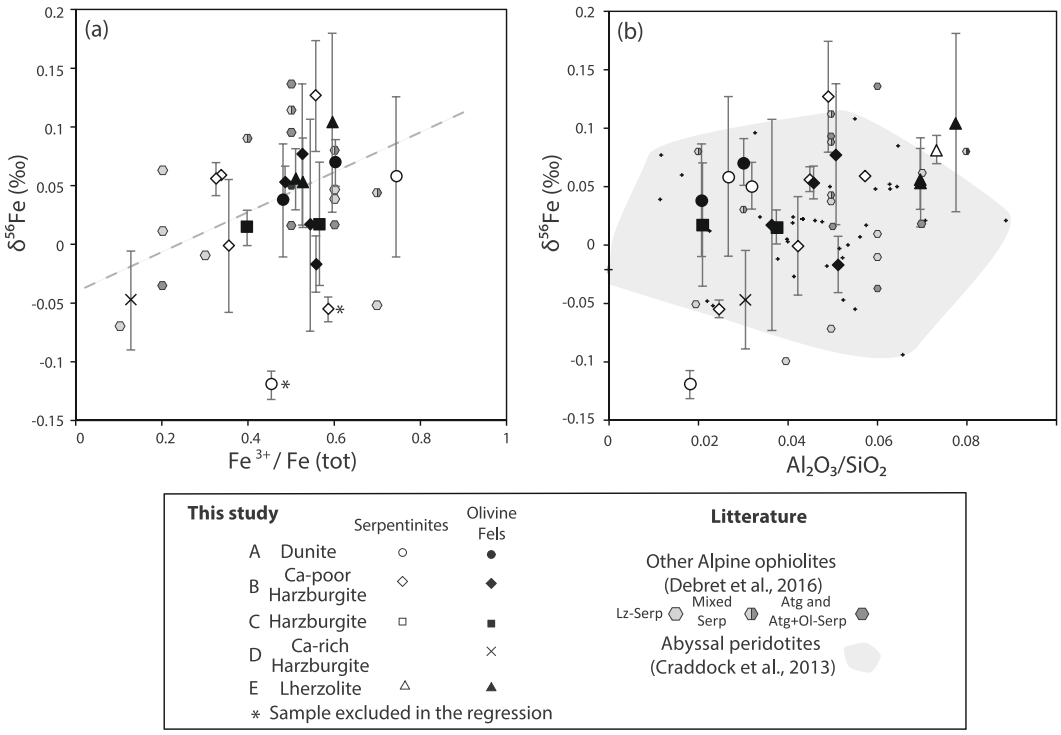

FIGURE 6 Binary diagrams showing: (a) $\delta^{56}Fe$ versus Fe^{3+}/Fe_{tot} and (b) $\delta^{56}Fe$ versus Al_2O_3/SiO_2. The linear regression in (a) as the following expression: $f(x) = 0.16x - 0.035$ with a r^2 of 0.28. $\delta^{56}Fe$ data for abyssal peridotites from Craddock et al. (2013) and data from other alpine localities (Lanzo, Monte-Maggiore, and Montgenèvre ophiolite; Debret et al., 2016) are shown as a comparison.

correlation coefficient is 0.28, which is relatively low. No correlation between $\delta^{56}Fe$ values and Al_2O_3/SiO_2 ratios is observed. Literature values show the same amount of variability and an absence of correlation for samples from various Alpine serpentinites and partially reacted serpentinites. The $\delta^{56}Fe$ values of serpentinites and olivine-talc fels do not show any correlation with the LOI or the metamorphic imprint within the Bergell contact aureole.

5.2.3 | Minor and trace element compositions

Similar compositions in minor elements are observed in the distinct serpentinites and olivine-talc fels groups. The samples have indeed a quite homogeneous NiO content with average values of 0.29 wt.% (0.18–0.49 wt.%). Generally, slightly higher NiO values were measured in dunites and Ca-poor harzburgites compared with lherzolites and harzburgites (Figure S6). Lherzolites and Ca-rich harzburgites display a higher MnO content (0.14 to 0.23 wt.%, average at 0.18 wt.%) than dunites and Ca-poor harzburgites (0.11 to 0.21 wt.%, average at 0.14 wt.%). There is a positive correlation between TiO_2 and Al_2O_3 contents, which increase from dunitic to lherzolitic rocks (Figure S6). The Ca-rich harzburgites are enriched in MnO but depleted in TiO_2 (below 0.03 wt.%). There is no correlation for any element with LOI or with the proximity to the intrusion.

Based upon minor elements characteristics, we show trace element compositions of serpentinites and olivine-talc fels within the Bergell aureole according to the rock types defined by their major element compositions (see Figure 4). They are displayed in Figures 7–9. Trace

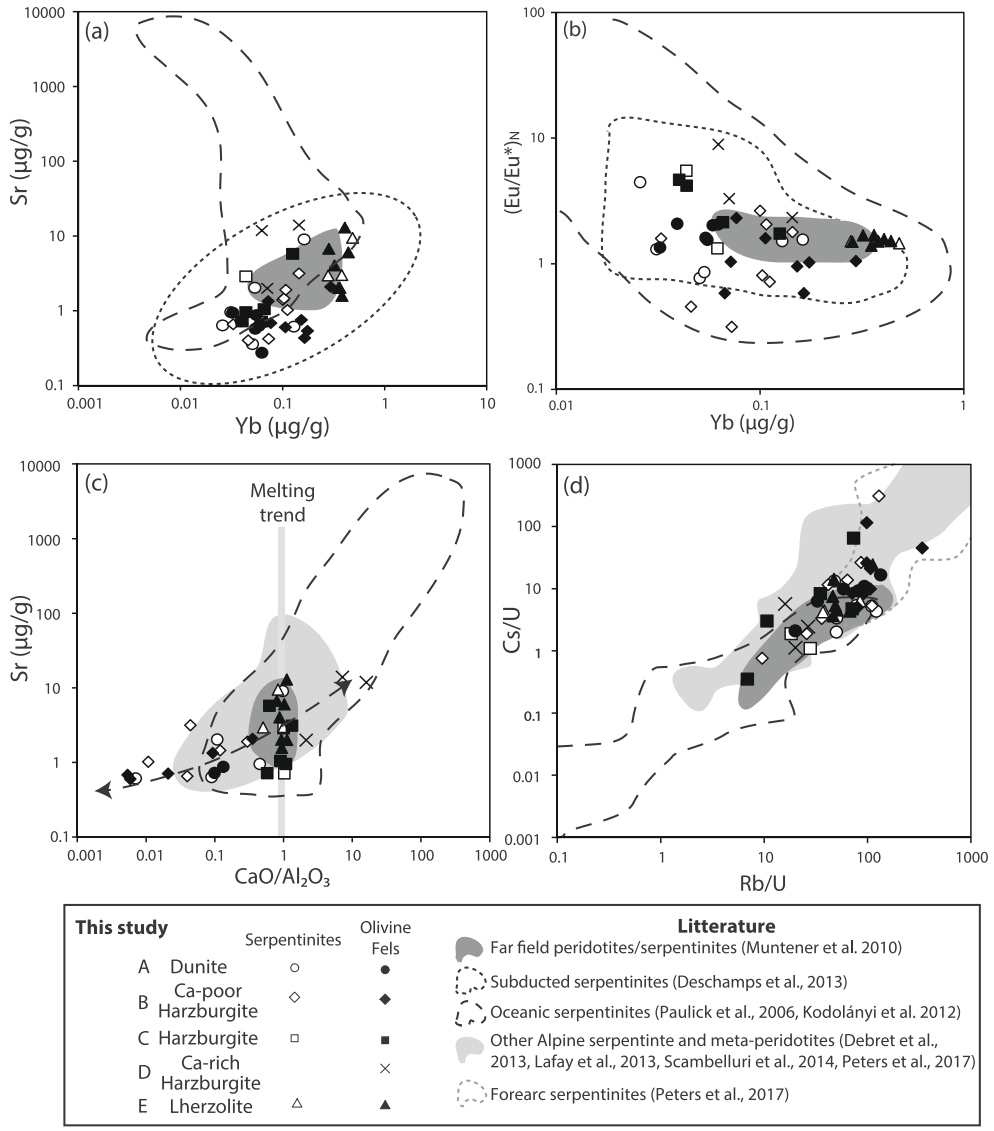

FIGURE 7 Binary diagrams showing (a) Sr versus Yb concentrations, (b) $(Eu/Eu^*)_N$ ratio versus Yb, $((Eu/Eu)_N^* = Eu/((Sm + Gd)/2))$ normalized to chondrite, (c) Sr content versus CaO/Al_2O_3 ratios, (d) Cs/U versus Rb/U demonstrating the consistency of trace element composition in each ultramafic rock groups. Note the peculiar trend between Sr content and CaO/Al_2O_3, the Ca-poor harzburgite being the more depleted rocks and the abyssal peridotites being extremely enriched in Sr. Symbol distinction was made based on major element geochemistry as defined in Figure 4, white and black correspond to serpentinites and olivine-talc fels, respectively. Data for from far-field peridotites/serpentinites (Müntener et al., 2010), data for subduction zone serpentinites (review from Deschamps et al., 2013), data for abyssal and mid-ocean-ridge (MOR) serpentinites (Kodolányi et al. 2012; Paulick et al., 2006), data for other meta-serpentinites and olivine-talc fels from other alpine localitie (Debret et al., 2013; Lafay et al., 2013; Peters et al., 2017; Scambelluri et al., 2014) and data for forearc serpentinites (Peters et al., 2017) are also reported. Dotted line in (c) is eyeball fit for Ca-poor and Ca-rich harzburgites.

element concentrations in serpentinites and olivine-talc fels show little variation within each rock classification, with a few exceptions. Lherzolites have higher concentrations of Sr and heavy rare earth elements (HREE) than all other rock types (Figures 7a,b and 8e). The (Eu/Eu*) ratios for serpentinites and olivine-talc fels are comparable with those reported for abyssal and subducted serpentinites and all trace element compositions fall within the range of values found in the literature data (refer to Deschamps et al., 2013, and reference therein). Rocks plotting on the melting trend in the CaO/Al_2O_3 diagram show concentrations of Sr between those of Ca-poor (low Sr content) and Ca-rich (high Sr content) harzburgites (Figure 7a). The distribution in Sr concentration seems to reflect mostly rock fertility (i.e., HREE and Al_2O_3) and correlates well with CaO enrichment (Figure 7c).

All chondrite-normalized REE patterns (McDonough & Sun, 1995) are slightly to strongly depleted (Figure 8)

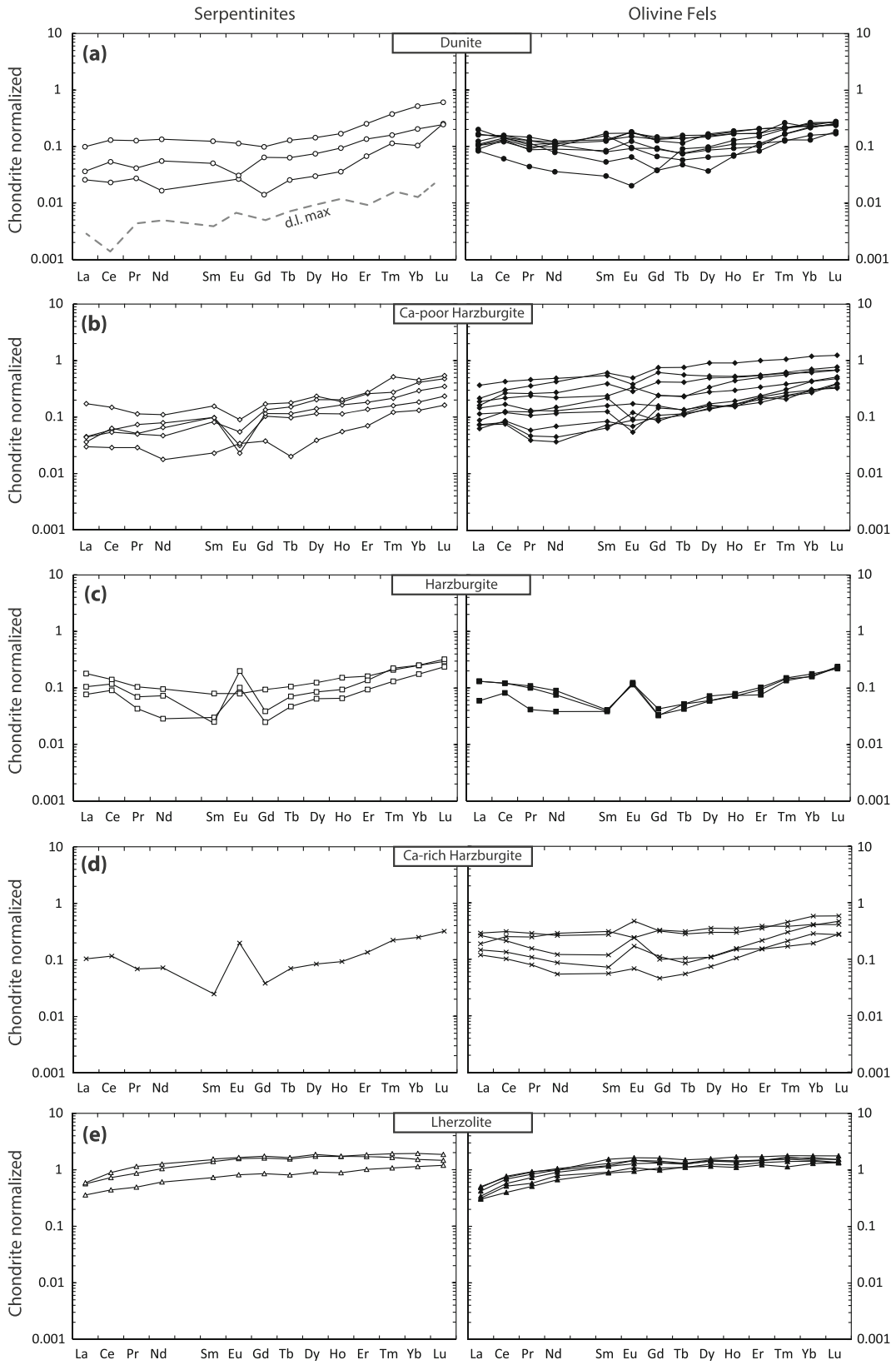

FIGURE 8 Chondrite-normalized REE patterns of serpentinites (left) and olivine fels (right) derived from dunites (a), Ca-poor harzburgites (b), harzburgites (c), Ca-rich harzburgites (d), and lherzolites (e), respectively demonstrating the good overlay between serpentinites and olivine-talc fels rocks and the consistency of REE composition in each rock group and the good correlation between REE patterns and the assumed rock types (more detail in the text). Normalization values are from McDonough and Sun (1995).

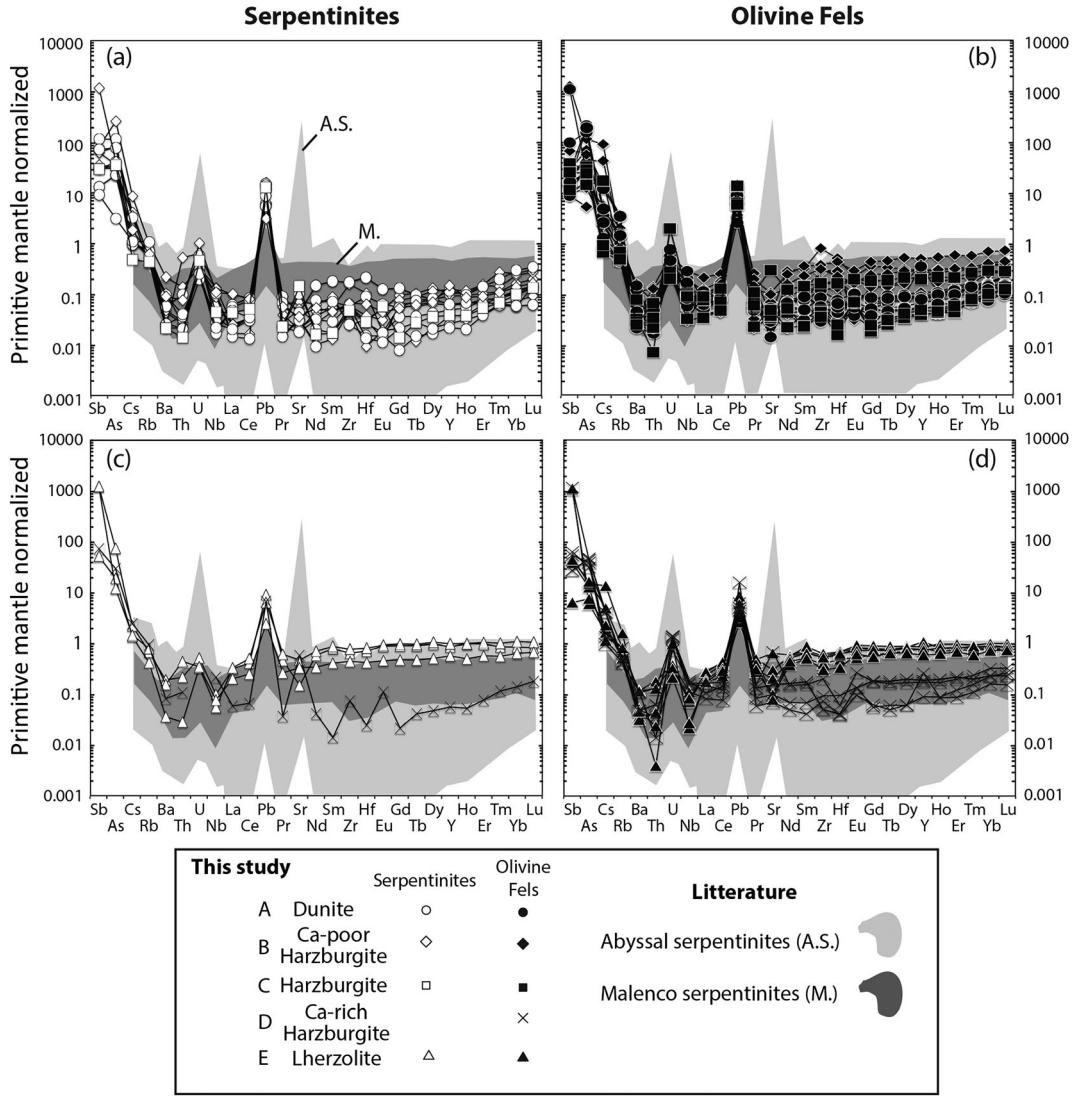

FIGURE 9 Primitive mantle normalized REE patterns of serpentinites (left) and olivine fels (right) from the Bergell contact aureole illustrating the good agreement between serpentinites and olivine-talc fels trace element compositions. Each panel was drawn for a different inferred mantle protolith: (a,b) dunites, Ca-poor harzburgites and harzburgites, and (c,d) lherzolites and Ca-rich harzburgites. Primitive mantle normalizing values from after McDonough and Sun (1995). Data for mid-ocean-ridge (MOR) and abyssal serpentinites (A.S. after Kodolányi et al. 2012) and literature values of serpentinites from the Malenco complex (M. after Müntener et al., 2010) are shown for comparison.

and can be divided into three groups whose variations in concentrations reflect the magmatic precursor. The first group, including dunites, harzburgites, and Ca-rich harzburgites, displays a concave-upward shape. Ca-poor harzburgites have a flat pattern or show a slight increase between light rare earth elements (LREE) and HREE (Figure 8b). Lherzolites are slightly depleted in LREE with a flat pattern between mid-REE and HREE exhibiting concentrations comparable with that of chondrite (Figure 8e). Harzburgites and Ca-rich harzburgites have similar REE patterns: They display a positive Eu anomaly and most are enriched in Sr (Figures 7c and 8c,d). Dunites and Ca-poor harzburgites display a negative Eu anomaly (Figures 7b and 8a,b) and are also characterized by depletion in Sr.

Extended trace element patterns, normalized to primitive mantle values of McDonough and Sun (1995), are characterized by a positive anomaly in Pb, comparable with abyssal peridotites (Deschamps et al., 2013; Kodolányi et al., 2012; Paulick et al., 2006), and to a lesser extent in U (Figure 9), irrespective of the rock types. Trace element patterns are similar for serpentinites and olivine-talc fels (Figure 9a vs. Figure 9b and Figure 9c vs. Figure 9d). All serpentinites and olivine-talc fels samples are enriched in some incompatible trace elements (Sb, Cs, and As) when compared with primitive

mantle, with a group of samples being highly enriched in Sb (1000× PM) and As (200× PM). These samples belong to several different rock types. Serpentinites and olivine-talc fels have moderate Sr/Pb ratios between 0.1 and 20, slightly lower than values of far-field serpentinites and about 1 to 3 orders of magnitude below the highest ratios reported for abyssal serpentinites (Figure 9). Enrichment in U (i.e., U/Th and U/Nb ratios) in contact-metamorphosed rocks with respect to mantle peridotite is similar to enrichment in far-field serpentinites and slightly serpentinized peridotites and to enrichment reported for other alpine ophiolites (Figure 9b and Figure 9c) but is usually a few orders of magnitude below the one reported for abyssal serpentinites. The Fe-poor serpentinites do not show any particular trace element signature.

6 | DISCUSSION

6.1 | Protolith compositions and metamorphic sequence

Mantle heterogeneities are well preserved in regional metamorphic serpentinites (Müntener & Hermann, 1996) despite serpentinization on the ocean floor and greenschist facies metamorphism. Our field work and petrographic study show that this is similar for rocks within the aureole (see also Evans, 1977; Müntener & Hermann, 1996; Trommsdorff & Evans, 1972) despite initial and subsequent contact metamorphism leading to serpentinites dehydration. Observed geochemical trends are not related to regional metamorphism and cannot be attributed to deserpentinization but are instead attributed to protolith heterogeneity. Herein, no systematic chemical changes were found in the aureole, besides loss of water by metamorphic reactions.

The rocks investigated in the present study cover a wide range of compositions reflecting the submeter to decameter-thick mantle layering formed by mantle processes, such as partial melting and refertilization (Müntener et al., 2010; Müntener & Hermann, 1996). These mantle rocks are recognizable throughout the aureole. This general feature is observed in abyssal serpentinites and in other Alpine serpentinites and metaperidotites (e.g., Debret et al., 2013; Lafay et al., 2013; Scambelluri et al., 2014). Indeed, the serpentinites within the aureole range from typical dunites to lherzolites and retain some of the hall-mark textures of oceanic serpentinization, such as mesh textures. Initial serpentine polymorphs (lizardite/chrysotile) obviously reacted to antigorite during Alpine regional metamorphism (Figure 10b), which reached temperatures of 400–450°C (Guntli & Liniger, 1989). Metamorphic diopside and olivine formed by brucite breakdown during the regional greenschist facies.

The contact metamorphic overprint is manifested by the simultaneous disappearance of clinopyroxene and appearance of tremolite (Figure 10a). The isograd of serpentinite breakdown to talc forms a sharp and sinuous boundary in the field and the complete transformation of most rocks occurs in less than a few tens of meters of this. At the lowest grade, a few talc + olivine veins crosscut the rocks, indicating that dehydration occurred preferentially where water could escape in veins (see Clément et al., 2019). We found a few serpentinite lenses up to a hundred meters from talc-in isograd. This serpentinite preservation could be due to kinetic inhibition of the talc-forming reaction or to fluid pressure increase during initial dehydration (Padrón-Navarta et al., 2011). Another simpler explanation could be, in the case of the Bergell aureole, the change in rock composition. Indeed, these serpentinite pods correspond to former dunitic rocks layers in harzburgitic rocks and they systematically show lower Fe contents, which results in slightly higher temperatures of serpentinite destabilization (Figure 11 and Supporting Information).

There is substantial recrystallization involving magnetite, as attested by a general change in magnetite grain size. Indeed, fine-grained magnetite occurring in the matrix after serpentinite breakdown (talc-in isograd) is due to ferric iron released by antigorite, as observed by Vieira Duarte et al. (2021) in hydrous ultramafic rocks from Cerro del Almirez. Aluminium released from antigorite produces chlorite, leading to its recrystallization (Padrón-Navarta et al., 2013). New olivine is formed by antigorite breakdown, leading to Jack straw olivine near the talc-in isograd (Figure 10b) and euhedral olivine throughout the contact aureole. The southeastern area studied is thus an excellent example of preservation of the original mantle heterogeneities (Preda-Rossa, Figure 2a).

6.2 | Mobility of elements, oxidation state, and iron isotopes during contact metamorphism

6.2.1 | Element mobility during contact metamorphism

The composition of the Malenco ultramafic rocks are similar to abyssal serpentinites (Deschamps et al., 2013; Kodolányi et al., 2012), with marked enrichments in Pb, U as well as in As, Sb, Ba, Rb, and Cs (Pettke et al., 2018) with respect to primitive mantle (Figure 9). With respect to concentrations in alkali elements, Cs and Rb, plot in

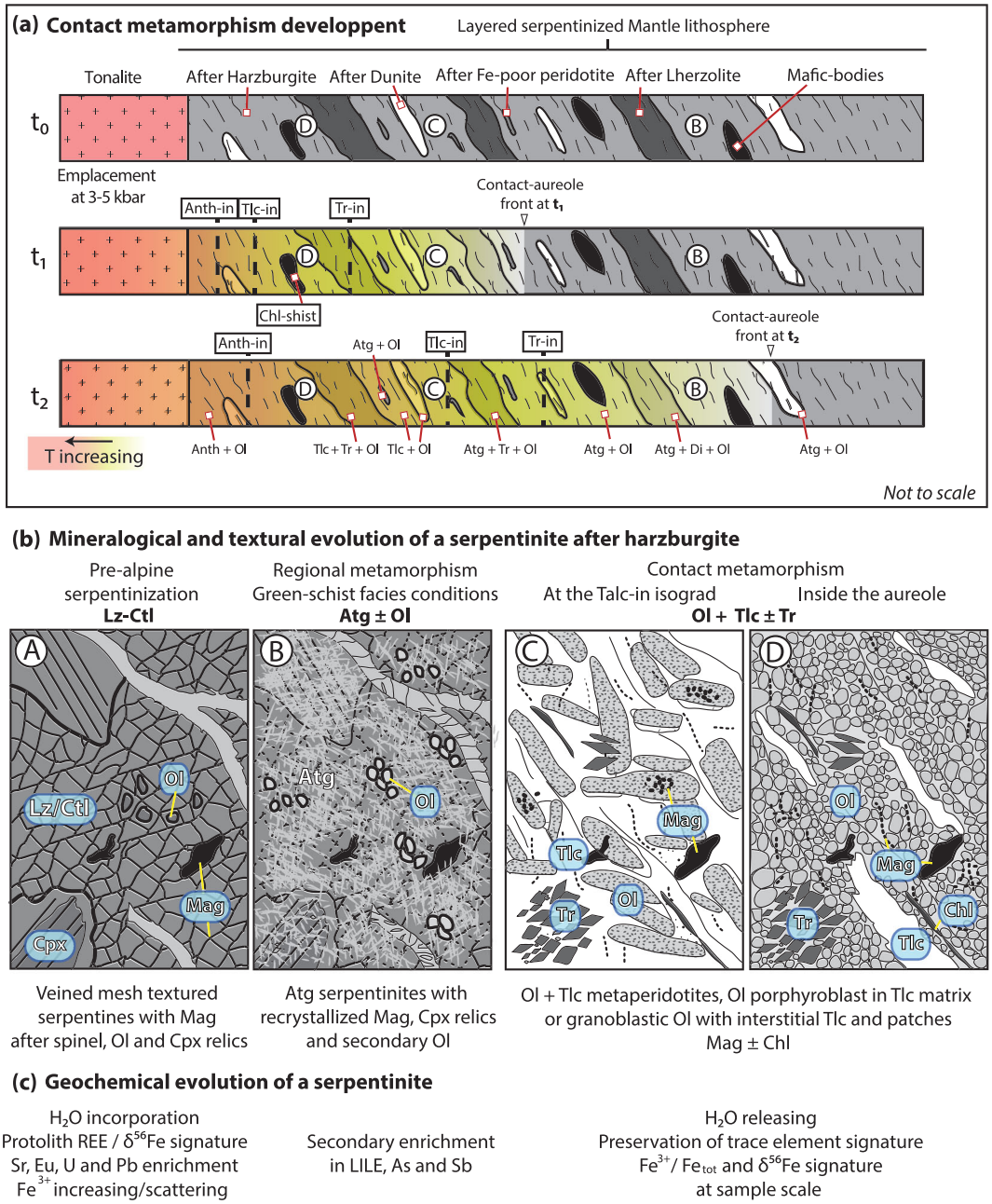

FIGURE 10 (a) Series of diagrams illustrating the thermal aureole of Bergell tonalite in a heterogeneous serpentinized ultramafic unit leading to the progressive displacement of metamorphic isograds until the actual (t_2) position; t_0 correspond to the time at which the intrusion take place in the serpentinite unit (after regional metamorphism). Primary layering controls metamorphic paragenesis and serpentinite chemical signature remains preserved. (b) Compilation sketch summarizing the textural evolution of metamorphosed peridotites from (a) mesh and bastite textured serpentinites mainly composed of lizardite and chrysotile after oceanic serpentinization (inspired by Rouméjon et al., 2018), (b) HT serpentinite marked by antigorite overprinting and the appearance of metamorphic olivine then olivine-talc fels and olivine-anthophyllite fels characterized by (c) coarse elongated tabular olivine in a talc matrix near the talc-in isograd and (d) a granoblastic texture and the presence of intergranular talc and talc patches inside the aureole. Atg: antigorite, Chl: Chlorite, Ctl: chrysotile, Lz: lizardite, Ol: olivine, Tlc: talc, Tr: tremolite

the fields of other Alpine ophiolites (Peters et al., 2017; Scambelluri et al., 2019). Enrichment in alkali and chalcophile elements was already present in the regional metamorphic serpentinites and is not further modified by the contact metamorphism. These chemical characteristics have been previously interpreted as a consequence of infiltration of sediment-derived fluids during subduction in other ophiolite settings (Deschamps et al., 2013; Lafay et al., 2013; Marchesi et al., 2013; Peters et al., 2017; Scambelluri et al., 2019; Savov et al., 2005).

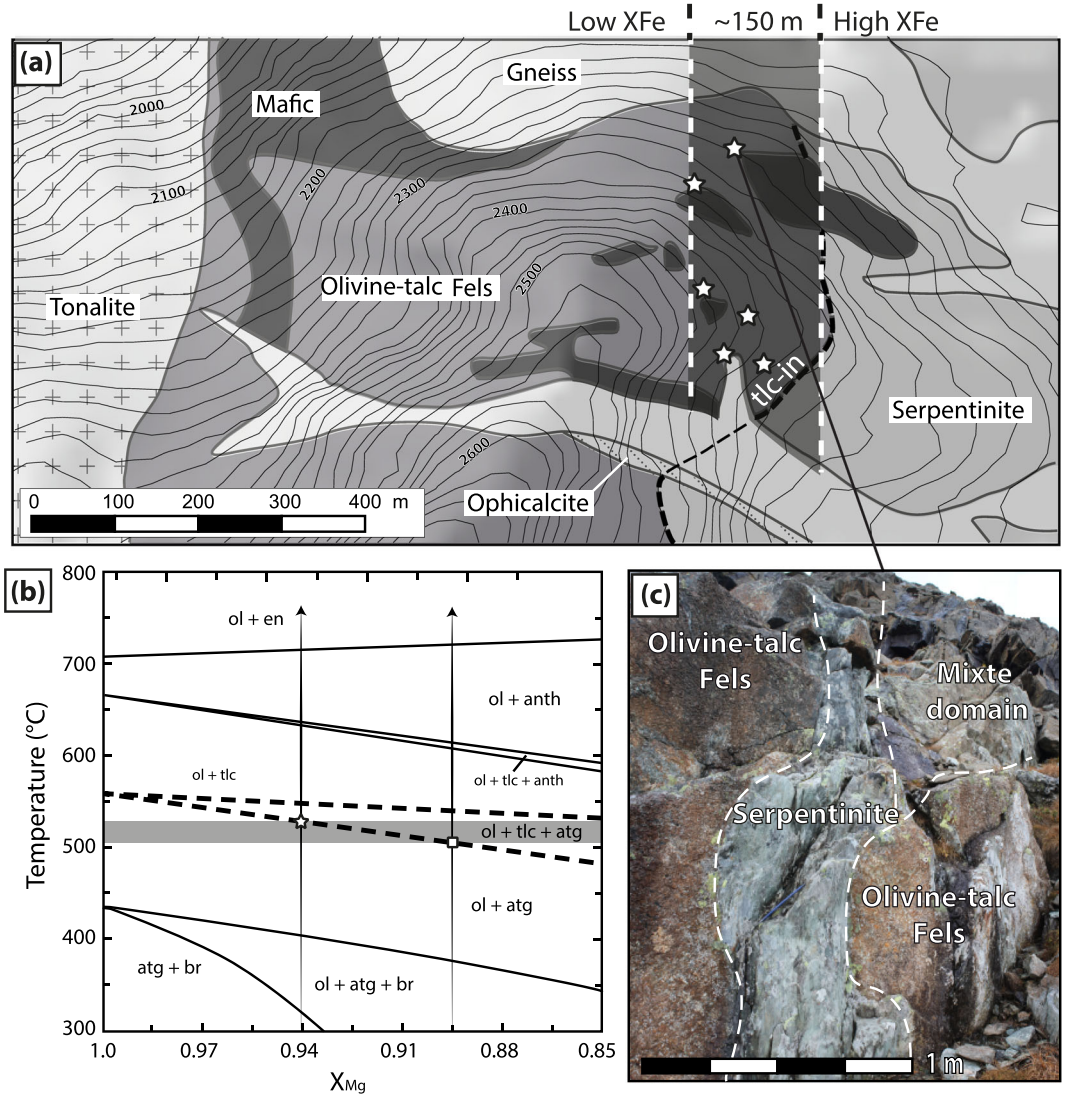

FIGURE 11 (a) Map of the north-western parts of the aureole where serpentinite bodies (white stars) were found within the olivine-talc fels, the shaded part corresponds to the domain between the first occurrence of talc and the disappearance of serpentinite bodies approaching the intrusion. (b) Isobaric T–X_{Mg} pseudosection at 0.4 GPa in the FMSH system considering an antigorite crystallography. The shaded area highlights the difference in temperature for talc appearance between Fe-poor serpentinite ($X_{Mg} \sim 0.94$) and an average Malenco serpentinite composition ($X_{Mg} \sim 0.90$), (the temperature difference represented here is 22°C and can reach 45°C for a X_{Mg} differences of 0.8). (c) Example of serpentinite lense (corresponding to sample 28) within olivine-talc fels (corresponding to sample 28b)

In Malenco, the serpentinites underwent accretion and metamorphism into greenschist facies. We conclude that the concentrations in LILE (e.g., Rb and Sr) and HREE (like Yb) largely reflect the inheritance of the protolith compositions, which in turn reflect mantle layering (as proposed in Figure 10), and the variable oceanic alteration by seawater (Scambelluri et al., 2014) before Alpine orogeny. Gabbro intrusions into the oceanic lithosphere, triggering and sustaining hydrothermal circulation and then alteration, may also lead to enrichment in fluid mobile elements (e.g., 1000 × As, Sb) (Deschamps et al., 2012).

Antigorite breakdown produces up to 250 kg/m^3 of water. The effect of this large amount of released water can be assessed with our data by comparing element compositions and isotopic compositions of serpentinites and olivine-talc fels (Figures 8 and 9). Surprisingly, we do not find any systematic differences in the chemical patterns, with the exception of the volatile loss reflected in the LOI values. Variations and characteristics of the element patterns are similar for both serpentinites and olivine-talc fels. Hence, we argue that any differences observed within each group—the serpentinites and the olivine-talc fels—reflect chemical differences inherited

from the mantle protolith and overprinted by oceanic serpentinization. Indeed, Sr and Eu display positive or negative anomalies, consistent with what is expected from mantle trends and similarly to samples from other localities in the Malenco ophiolite (Müntener et al., 2010) and to abyssal serpentinites (Kodolányi et al., 2012). Hence, depletion or enrichment in CaO, relative to the mantle trend, in some of the Malenco samples involves either a leaching or an addition of Ca from/to the original peridotite (Figure 4a,b). The trend is visible in low-grade and high-grade samples. We conclude that they reflect intensive fluid–rock interaction that occurred during serpentinization. Enrichments in Sr and Ca towards Ca-rich harzburgites could be a consequence of refertilization due to plagioclase crystallization as suggested by Müntener et al., (2010) and Niu et al. (1997).

Overall, no significant changes in major, minor, trace, or REE element concentrations due to dehydration during antigorite breakdown to olivine and talc were identified in the contact aureole of the Bergell intrusion. All chemical heterogeneities documented in the Malenco ultramafic rocks are either due to mantle partial melting, refertilization, or ocean floor serpentinization.

6.2.2 | Behaviour of Fe and Fe isotope composition during serpentine breakdown

Ocean floor serpentinization produces serpentinites with higher Fe^{3+}/Fe_{tot} ratios than their precursor mantle rocks that contained predominantly ferrous iron (Evans, 2008). Minerals produced during serpentinization of olivine, such as serpentine and magnetite, or during alteration of Cr-spinel, such as ferritchromite, contain a significant amount of ferric iron. For serpentine minerals, the amount of ferric iron is dependent on the degree of alteration and the temperature of serpentinization reaction (Andreani et al., 2013; Klein et al., 2014). In that sense, whole rock $Fe^{3+}/Fe_{(tot)}$ ratio can be used as a proxy of hydration degree in abyssal systems (Evans, 2008), even if it remains non-linear and variable according to the geodynamic context (Frost et al., 2013).

The high Fe^{3+}/Fe_{tot} ratios (up to 0.8) measured in most of the Malenco rocks likely reflect an important serpentinization degree of the Malenco units, during which Fe^{3+} was produced and included into serpentine minerals and magnetite prior to contact metamorphism episode. Despite the high degree of oxidation, no haematite was observed. Here we show that serpentine breakdown during contact metamorphism did not change the Fe^{3+}/Fe^{2+} ratio, since the observed Fe^{3+}/Fe_{tot} variations are similar for serpentinites and olivine-talc fels. Based on the preservation of this Fe^{3+}/Fe^{2+} ratio during massif dehydration due to contact metamorphism, it seems likely that this ratio was also not modified during earlier Alpine prograde metamorphism that produced metamorphic antigorite, diopside, and some olivine. This would hence imply that the observed variations are likely related to the initial mantle lithology and to the heterogeneous initial serpentinization process, which resulted in from complete alteration to preservation of nearly 90% of the mantle mineralogy (Müntener et al., 2010). The heterogeneous nature of serpentinization will lead to the formation of rock-dominated and fluid-dominated domains (Paulick et al., 2006). In addition, experimental and thermodynamic investigations have shown that kinetics of serpentinization, as well as temperature, vary strongly (Allen & Seyfried, 2003). A lower Fe^{3+}/Fe_{tot} is predicted in serpentinites formed from clinopyroxene-rich rocks than in serpentinite formed from olivine-rich mantle rocks, whatever the serpentinization temperature (Klein et al., 2013).

$\delta^{56}Fe$ values of serpentinites and olivine-talc fels range between −0.12 to 0.14 ‰ and are within the overall range of $\delta^{56}Fe$ values reported for upper mantle and abyssal peridotites (−0.10 to +0.12 ‰, Craddock et al., 2013; Weyer & Ionov, 2007). No correlation exists between Fe isotope compositions and enrichment in LOI and in LILE, or with the increase in U/Th and U/Nb ratios, factors that monitor the progress of serpentinization (e.g., Deschamps et al., 2013; Kodolányi et al., 2012). There is also no correlation between Fe isotope composition and Al_2O_3/SiO_2. Nevertheless, a slight positive correlation exists between the $\delta^{56}Fe$ values and the Fe^{3+}/Fe_{tot} ratios, especially for the olivine-talc fels (Figure 5a), likely indicating a very small enrichment in ^{56}Fe with oxidation degree. As $\delta^{56}Fe$ values ranges are similar for the serpentinites and the olivine-talc fels, we can hypothesize that the very small isotopic enrichment may be related to (1) the primary compositions of the mantle rocks and (2) the previous processes, such as fluid–rock interaction processes that monitor the progress of serpentinization, and not to contact metamorphism. Indeed, Craddock et al. (2013) demonstrated that mantle peridotites preserved a chondritic Fe isotope composition and small variation may reflect the degree of melting or subtle differences, such as oxidation state and fugacity, in mantle domains. In addition, similar interpretations were suggested for high pressure rocks in Groix (Brittany, France, in El Korh et al., 2017). The lack of differences in $\delta^{56}Fe$ values as a function of metamorphic grade in the contact aureole (Figure 10c) may suggest that no fractionation occurs with increasing temperature. We conclude that dehydration reflecting a mass loss of 10% is not able to change the $\delta^{56}Fe$ values nor the oxidation state.

7 | CONCLUSIONS

The contact aureole of the Bergell intrusion represents a remarkable field laboratory to investigate progressive serpentinite dehydration, since chemical variations can be studied along short distances over which major metamorphic gradients occur. Serpentinites to olivine-talc fels and anthophyllite-talc fels transitions within the Bergell contact aureole do not lead to visible major and trace element changes. In fact, no chemical variations were documented by our data, with the exception of a decrease in volatile content, reflected by LOI. The observed chemical distributions in ultramafic rocks reflect the differences in protolith nature and in the signature inherited from ocean floor serpentinization processes. The protolith remains visible through its mineralogy and major element geochemistry.

Debret et al. (2014) proposed that progressive serpentinite dehydration in convergent systems is accompanied by a decrease in bulk rock Fe^{3+}/Fe_{tot} ratios due to the production of oxidizing fluids. Their hypotheses are based on an observed decrease in magnetite content at the lizardite-antigorite transition and during early stage of metamorphic olivine formation. Conversely, Piccoli et al., 2019 argued for the release of reduced fluids on the basis of phase equilibrium calculations and as sulfides-oxides-alloys are commonly observed in ophiolites. Our study agrees with Piccoli et al. (2019) in that no change in Fe^{3+}/Fe_{tot} ratios was observed during the breakdown of serpentine. Hence the massive amount of fluid loss does not significantly change the oxidation state at that point. Similar conclusion were obtained at the Cerro de Almirez and Alpine ultramafic bodies and from thermodynamic calculations up to eclogite facies conditions (Bretscher et al., 2018; Evans & Frost, 2020; Padrón-Navarta et al., 2011; Piccoli et al., 2019; Scambelluri et al., 2014). Instead, in the case of the Malenco serpentinites, the protolith composition and the serpentinization degree are the main parameters controlling the Fe^{3+}/Fe_{tot} ratios.

We conclude that the original signature and distribution of the peridotites geochemistry has a strong resilience to protracted metamorphic events. The potential geochemical changes and isotopic fractionation accompanying antigorite breakdown in ophiolites must be considered according a great importance to the inherited serpentinite composition.

ACKNOWLEDGMENTS

Funding from Schweizerischer Nationalfonds zur Förderung der Wissenschaftlichen Forschung grant 200021-153094 and 200020-172513 helped support this research. The authors are grateful to Othmar Müntener for detailed discussions prior to submission. We thank Amélie Didier for help during sampling in the field and A. Gannoun for his help during Fe isotopes analyses. We thank the anonymous reviewers for their constructive comments and suggestions which have improved the quality of the article. We particularly thank Professor Katy Evans for her insightfull comments and corrections and her remarkable work in monitoring the article during the editing process.

ORCID

Romain Lafay https://orcid.org/0000-0001-6295-5871

REFERENCES

Allen, D. E., & Seyfried, W. E. (2003). Compositional controls on vent fluids from ultramafic-hosted hydrothermal systems at mid-ocean ridges: An experimental study at 400°C, 500 bars. *Geochimica et Cosmochimica Acta*, *67*(8), 1531–1542. https://doi.org/10.1016/S0016-7037(02)01173-0

Andreani, M., Daniel, I., & Pollet-Villard, M. (2013). Aluminum speeds up the hydrothermal alteration of olivine. *American Mineralogist*, *98*(10), 1738–1744. https://doi.org/10.2138/am.2013.4469

Beard, B. L., Johnson, C. M., Von Damm, K. L., & Poulson, R. L. (2003). Iron isotope constraints on Fe cycling and mass balance in oxygenated Earth oceans. *Geology*, *31*(7), 629–632. https://doi.org/10.1130/0091-7613(2003)031<0629:IICOFC>2.0.CO;2

Bretscher, A., Hermann, J., & Pettke, T. (2018). The influence of oceanic oxidation on serpentinite dehydration during subduction. *Earth and Planetary Science Letters*, *499*, 173–184. https://doi.org/10.1016/j.epsl.2018.07.017

Bromiley, G. D., & Pawley, A. R. (2003). The stability of antigorite in the systems $MgO\text{-}SiO_2\text{-}H_2O$ (MSH) and $MgO\text{-}Al_2O_3\text{-}SiO_2\text{-}H_2O$ (MASH): The effects of Al^{3+} substitution on high-pressure stability. *American Mineralogist*, *88*(1), 99–108. https://doi.org/10.2138/am-2003-0113

Busigny, V., Planavsky, N. J., Jézéquel, D., Crowe, S., Louvat, P., Moureau, J., Viollier, E., & Lyons, T. W. (2014). Iron isotopes in an Archean ocean analogue. *Geochimica et Cosmochimica Acta*, *133*, 443–462. https://doi.org/10.1016/j.gca.2014.03.004

Chernosky, J., Day, H. W., & Caruso, L. (1985). Equilibria in the system $MgO\text{-}SiO_2\text{-}H_2O$; experimental determination of the stability of Mg-anthophyllite. *American Mineralogist*, *70*(3–4), 223–236.

Clément, M., Padrón-Navarta, J. A., & Tommasi, A. (2019). Interplay between fluid extraction mechanisms and antigorite dehydration reactions (Val Malenco, Italian Alps). *Journal of Petrology*, *60*(10), 1935–1962. https://doi.org/10.1093/petrology/egz058

Craddock, P. R., & Dauphas, N. (2011). Iron isotopic compositions of geological reference materials and chondrites. *Geostandards and Geoanalytical Research*, *35*(1), 101–123. https://doi.org/10.1111/j.1751-908X.2010.00085.x

Craddock, P. R., Warren, J. M., & Dauphas, N. (2013). Abyssal peridotites reveal the near-chondritic Fe isotopic composition of the Earth. *Earth and Planetary Science Letters*, *365*, 63–76. https://doi.org/10.1016/j.epsl.2013.01.011

Dauphas, N., Craddock, P. R., Asimow, P. D., Bennett, V. C., Nutman, A. P., & Ohnenstetter, D. (2009). Iron isotopes may reveal the redox conditions of mantle melting from Archean to present. *Earth and Planetary Science Letters*, *288*(1–2), 255–267. https://doi.org/10.1016/j.epsl.2009.09.029

Dauphas, N., Van Zuilen, M., Wadhwa, M., Davis, A. M., Marty, B., & Janney, P. E. (2004). Clues from Fe isotope variations on the origin of early Archean BIFs from Greenland. *Science*, *306*(5704), 2077–2080. https://doi.org/10.1126/science.1104639

Davidson, C., Rosenberg, C., & Schmid, S. (1996). Symmagmatic folding of the base of the Bergell pluton, Central Alps. *Tectonophysics*, *265*(3–4), 213–238. https://doi.org/10.1016/S0040-1951(96)00070-4

Debret, B., Andreani, M., Godard, M., Nicollet, C., Schwartz, S., & Lafay, R. (2013). Trace element behavior during serpentinization/de-serpentinization of an eclogitized oceanic lithosphere: A LA-ICPMS study of the Lanzo ultramafic massif (Western Alps). *Chemical Geology*, *357*, 117–133. https://doi.org/10.1016/j.chemgeo.2013.08.025

Debret, B., Andreani, M., Muñoz, M., Bolfan-Casanova, N., Carlut, J., Nicollet, C., Schwartz, S., & Trcera, N. (2014). Evolution of Fe redox state in serpentine during subduction. *Earth and Planetary Science Letters*, *400*, 206–218. https://doi.org/10.1016/j.epsl.2014.05.038

Debret, B., Millet, M.-A., Pons, M.-L., Bouilhol, P., Inglis, E., & Williams, H. (2016). Isotopic evidence for iron mobility during subduction. *Geology*, *44*(3), 215–218. https://doi.org/10.1130/G37565.1

Debret, B., & Sverjensky, D. (2017). Highly oxidising fluids generated during serpentinite breakdown in subduction zones. *Scientific Reports*, *7*(1), 1–6.

Decrausaz, T., Müntener, O., Manzotti, P., Lafay, R., & Spandler, C. (2021). Fossil oceanic core complexes in the Alps. New field, geochemical and isotopic constraints from the Tethyan Aiguilles Rouges Ophiolite (Val d'Hérens, Western Alps, Switzerland). *Schweizerische Mineralogische und Petrographische Mitteilungen*, *114*(1), 1–27. https://doi.org/10.1186/s00015-020-00380-4

Deschamps, F., Godard, M., Guillot, S., Chauvel, C., Andreani, M., Hattori, K., Wunder, B., & France, L. (2012). Behavior of fluid-mobile elements in serpentines from abyssal to subduction environments: Examples from Cuba and Dominican Republic. *Chemical Geology*, *312-313*, 93–117. https://doi.org/10.1016/j.chemgeo.2012.04.009

Deschamps, F., Godard, M., Guillot, S., & Hattori, K. (2013). Geochemistry of subduction zone serpentinites: A review. *Lithos*, *178*, 96–127. https://doi.org/10.1016/j.lithos.2013.05.019

Dilissen, N., Hidas, K., Garrido, C. J., Kahl, W. A., Sánchez-Vizcaíno, V. L., & Padrón-Navarta, J. A. (2018). Textural evolution during high-pressure dehydration of serpentinite to peridotite and its relation to stress orientations and kinematics of subducting slabs: Insights from the Almirez ultramafic massif. *Lithos*, *320-321*, 470–489. https://doi.org/10.1016/j.lithos.2018.09.033

Dolejš, D., & Manning, C. E. (2010). Thermodynamic model for mineral solubility in aqueous fluids: Theory, calibration and application to model fluid-flow systems. *Geofluids*, *10*(1–2), 20–40.

El Korh, A., Luais, B., Deloule, E., & Cividini, D. (2017). Iron isotope fractionation in subduction-related high-pressure metabasites (Ile de Groix, France). *Contributions to Mineralogy and Petrology*, *172*(6), 41. https://doi.org/10.1007/s00410-017-1357-x

Eugster, H. P., & Baumgartner, L. (1987). Mineral solubilities and speciation in supercritical metamorphic fluids. In *Thermodynamic modeling of geologic materials* (pp. 367–404). De Gruyter.

Evans, B. W. (1977). Metamorphism of alpine peridotite and serpentinite. *Annual Review of Earth and Planetary Sciences*, *5*(1), 397–447. https://doi.org/10.1146/annurev.ea.05.050177.002145

Evans, B. W. (2008). Control of the products of serpentinization by the $Fe^{2+}Mg_{-1}$ exchange potential of olivine and orthopyroxene. *Journal of Petrology*, *49*(10), 1873–1887. https://doi.org/10.1093/petrology/egn050

Evans, B. W., & Trommsdorff, V. (1974). On elongate olivine of metamorphic origin. *Geology*, *2*(3), 131–132. https://doi.org/10.1130/0091-7613(1974)2<131:OEOOMO>2.0.CO;2

Evans, K. A., & Frost, B. R. (2020). Deserpentinization in subduction zones as a source of oxidation in arcs: A reality check. *Journal of Petrology*, *62*(1), 1–32.

Ferrand, T. P. (2019). Seismicity and mineral destabilizations in the subducting mantle up to 6 GPa, 200 km depth. *Lithos*, *334*, 205–230.

Frost, B. R., & Beard, J. S. (2007). On silica activity and serpentinization. *Journal of Petrology*, *48*(7), 1351–1368.

Frost, B. R., Evans, K. A., Swapp, S. M., Beard, J. S., & Mothersole, F. E. (2013). The process of serpentinization in dunite from New Caledonia. *Lithos*, *178*, 24–39. https://doi.org/10.1016/j.lithos.2013.02.002

Ganzhorn, A. C., Pilorgé, H., & Reynard, B. (2019). Porosity of metamorphic rocks and fluid migration within subduction interfaces. *Earth and Planetary Science Letters*, *522*, 107–117. https://doi.org/10.1016/j.epsl.2019.06.030

Guntli, P., & Liniger, M. (1989). Metamorphose in der Margna-Decke im Bereich Piz da la Margna und Piz Fedoz (Oberengadin). *Schweizerische Mineralogische und Petrographische Mitteilungen*, *69*(2), 289–301.

Hirth, G., & Guillot, S. (2013). Rheology and tectonic significance of serpentinite. *Elements*, *9*(2), 107–113. https://doi.org/10.2113/gselements.9.2.107

Jackson, S. E. (2008). *LAMTRACE data reduction software for LA-ICP-MS: Laser ablation ICP-MS in the earth sciences: Current practices and outstanding issues* (pp. 305–307). Mineralogical Association of Canada.

Jäger, E. (1973). Die alpine Orogenese im Lichte der radiometrischen Altersbestimmung. *Eclogae Geologicae Helvetiae*, *66*, 11–21.

Jagoutz, E., Palme, H., Baddenhausen, H., Blum, K., Cendales, M., Dreibus, G., Spettel, B., Lorenz, V. Wänke, H. (1979). The abundances of major, minor and trace elements in the earth's mantle as derived from primitive ultramafic nodules. In Lunar and Planetary Science Conference Proceedings, *10*, 2031–2050.

Klein, F., Bach, W., Humphris, S. E., Kahl, W.-A., Jöns, N., Moskowitz, B., & Berquó, T. S. (2014). Magnetite in seafloor serpentinite—Some like it hot. *Geology*, *42*(2), 135–138. https://doi.org/10.1130/G35068.1

Klein, F., Bach, W., & McCollom, T. M. (2013). Compositional controls on hydrogen generation during serpentinization of

ultramafic rocks. *Lithos*, *178*, 55–69. https://doi.org/10.1016/j.lithos.2013.03.008

Kodolányi, J., Pettke, T., Spandler, C., Kamber, B. S., & Gméling, K. (2012). Geochemistry of ocean floor and fore-arc serpentinites: Constraints on the ultramafic input to subduction zones. *Journal of Petrology*, *53*(2), 235–270.

Lafay, R., Baumgartner, L. P., Putlitz, B., & Siron, G. (2019). Oxygen isotope disequilibrium during serpentinite dehydration. *Terra Nova*, *31*(2), 94–101. https://doi.org/10.1111/ter.12373

Lafay, R., Deschamps, F., Schwartz, S., Guillot, S., Godard, M., Debret, B., & Nicollet, C. (2013). High-pressure serpentinites, a trap-and-release system controlled by metamorphic conditions: Example from the Piedmont zone of the western Alps. *Chemical Geology*, *343*, 38–54. https://doi.org/10.1016/j.chemgeo.2013.02.008

Marchesi, C., Garrido, C. J., Padrón-Navarta, J. A., Sánchez-Vizcaíno, V. L., & Gómez-Pugnaire, M. T. (2013). *Element mobility from seafloor serpentinization to high-pressure dehydration of antigorite in subducted serpentinite: Insights from the Cerro del Almirez ultramafic massif (southern Spain)* (Vol. 178, pp. 128–142). Lithos.

McDonough, W. F., & Sun, S.-S. (1995). The composition of the earth. *Chemical Geology*, *120*, 223–253. https://doi.org/10.1016/0009-2541(94)00140-4

Montrasio, A., Trommsdorff, V., & Hermann, J. (2005). Carta geologica della Valmalenco: Consiglio Nazionale delle Ricerche, Istituto per la dinamica dei processi, scale 1:25,000, 1 sheet.

Müntener, O., & Hermann, J. (1996). The Val Malenco lower crust-upper mantle complex and its field relations (Italian Alps). *Schweizerische Mineralogische und Petrographische Mitteilungen*, *76*(3), 475–500.

Müntener, O., & Hermann, J. (2001). The role of lower crust and continental upper mantle during formation of non-volcanic passive margins: Evidence from the Alps. *Geological Society, London, Special Publications*, *187*(1), 267–288. https://doi.org/10.1144/GSL.SP.2001.187.01.13

Müntener, O., Manatschal, G., Desmurs, L., & Pettke, T. (2010). Plagioclase peridotites in ocean–continent transitions: Refertilized mantle domains generated by melt stagnation in the shallow mantle lithosphere. *Journal of Petrology*, *51*(1–2), 255–294. https://doi.org/10.1093/petrology/egp087

Niu, Y., Langmuir, C. H., & Kinzler, R. J. (1997). The origin of abyssal peridotites: A new perspective. *Earth and Planetary Science Letters*, *152*(1–4), 251–265. https://doi.org/10.1016/S0012-821X(97)00119-2

Padrón-Navarta, J. A., Lopez Sanchez-Vizcaino, V., Garrido, C. J., & Gómez-Pugnaire, M. T. (2011). Metamorphic record of high-pressure dehydration of antigorite serpentinite to chlorite harzburgite in a subduction setting (Cerro del Almirez, Nevado-Filabride Complex, Southern Spain). *Journal of Petrology*, *52*(10), 2047–2078. https://doi.org/10.1093/petrology/egr039

Padrón-Navarta, J. A., Sánchez-Vizcaíno, V. L., Hermann, J., Connolly, J. A., Garrido, C. J., Gómez-Pugnaire, M. T., & Marchesi, C. (2013). Tschermak's substitution in antigorite and consequences for phase relations and water liberation in high-grade serpentinites. *Lithos*, *178*, 186–196. https://doi.org/10.1016/j.lithos.2013.02.001

Paulick, H., Bach, W., Godard, M., De Hoog, J., Suhr, G., & Harvey, J. (2006). Geochemistry of abyssal peridotites (Mid-Atlantic Ridge, 15 20′ N, ODP Leg 209): Implications for fluid/rock interaction in slow spreading environments. *Chemical Geology*, *234*(3–4), 179–210. https://doi.org/10.1016/j.chemgeo.2006.04.011

Peters, D., Bretscher, A., John, T., Scambelluri, M., & Pettke, T. (2017). Fluid-mobile elements in serpentinites: Constraints on serpentinisation environments and element cycling in subduction zones. *Chemical Geology*, *466*, 654–666. https://doi.org/10.1016/j.chemgeo.2017.07.017

Pettke, T., Kodolányi, J., & Kamber, B. S. (2018). From ocean to mantle: new evidence for U-cycling with implications for the HIMU source and the secular Pb isotope evolution of Earth's mantle. *Lithos*, *316-317*, 66–76. https://doi.org/10.1016/j.lithos.2018.07.010

Pfiffner, M., & Weiss, M. (1994). Strukturelle und petrographische Untersuchungen im Grenzbereich Penninikum-Unterostalpin am Südostrand des Bergell-Plutons (Val Masino, Italien). *Schweizerische Mineralogische und Petrographische Mitteilungen*, *74*(2), 245–264.

Picazo, S. M., Ewing, T. A., & Müntener, O. (2019). Paleocene metamorphism along the Pennine–Austroalpine suture constrained by U–Pb dating of titanite and rutile (Malenco, Alps). *Swiss Journal of Geosciences*, *112*(2), 517–542. https://doi.org/10.1007/s00015-019-00346-1

Piccoli, F., Hermann, J., Pettke, T., Connolly, J., Kempf, E., & Duarte, J. V. (2019). Subducting serpentinites release reduced, not oxidized, aqueous fluids. *Scientific Reports*, *9*(1), 1–7.

Reusser, C.E. (1987). Phasenbeziehungen im Tonalit der Bergeller Intrusion: ETH Zürich, Thèse de doctorat.

Reynard, B. (2013). Serpentine in active subduction zones. *Lithos*, *178*, 171–185. https://doi.org/10.1016/j.lithos.2012.10.012

Rouméjon, S., Früh-Green, G. L., Orcutt, B. N., & the IODP Expedition 357 Science Party. (2018). Alteration heterogeneities in peridotites exhumed on the Southern Wall of the Atlantis massif (IODP expedition 357). *Journal of Petrology*, *59*(7), 1329–1358. https://doi.org/10.1093/petrology/egy065

Rutter, E., & Brodie, K. H. (1988). Experimental "sytectonic" dehydration of serpentinite under conditions of controlled pore water pressure. *Journal of Geophysical Research - Solid Earth*, *93*(B5), 4907–4932. https://doi.org/10.1029/JB093iB05p04907

Samperton, K., Schoene, B., & Annen, C. (2015). How to build a mid-crustal intrusive suite: geologic mapping, U-Pb geo-/thermochronology, and thermal modeling of the Bergell Intrusion, Central Alps: Presented at 2015 Fall Meeting, AGU, San Francisco, California, p. 14–18 December.

Savov, I. P., Ryan, J. G., D'Antonio, M., Kelley, K., & Mattie, P. (2005). Geochemistry of serpentinized peridotites from the Mariana Forearc Conical Seamount, ODP Leg 125: Implications for the elemental recycling at subduction zones. *Geochemistry, Geophysics, Geosystems*, *6*(4). https://doi.org/10.1029/2004GC000777

Scambelluri, M., Cannaò, E., & Gilio, M. (2019). The water and fluid-mobile element cycles during serpentinite subduction. A review. *European Journal of Mineralogy*, *31*(3), 405–428.

Scambelluri, M., Pettke, T., Rampone, E., Godard, M., & Reusser, E. (2014). Petrology and trace element budgets of high-pressure peridotites indicate subduction dehydration of serpentinized mantle (Cima di Gagnone, Central Alps, Switzerland). *Journal of Petrology*, *55*(3), 459–498. https://doi.org/10.1093/petrology/egt068

Scambelluri, M., Rampone, E., & Piccardo, G. B. (2001). Fluid and element cycling in subducted serpentinite: A trace-element study of the Erro–Tobbio high-pressure ultramafites (Western Alps, NW Italy). *Journal of Petrology*, *42*(1), 55–67. https://doi.org/10.1093/petrology/42.1.55

Trommsdorff, V., & Connolly, J. A. (1996). The ultramafic contact aureole about the Bregaglia (Bergell) tonalite: Isograds and a thermal model. *Schweizerische Mineralogische und Petrographische Mitteilungen*, *76*, 537–547.

Trommsdorff, V., & Evans, B. W. (1972). Progressive metamorphism of antigorite schist in the Bergell tonalite aureole (Italy). *American Journal of Science*, *272*(5), 423–437. https://doi.org/10.2475/ajs.272.5.423

Ulmer, P., & Trommsdorff, V. (1995). Serpentine stability to mantle depths and subduction-related magmatism. *Science*, *268*(5212), 858–861. https://doi.org/10.1126/science.268.5212.858

Vieira Duarte, J. F., Piccoli, F., Pettke, T., & Hermann, J. (2021). Textural and geochemical evidence for magnetite production upon antigorite breakdown during subduction. *Journal of Petrology*, *62*(10), egab053. https://doi.org/10.1093/petrology/egab053

Vils, F., Müntener, O., Kalt, A., & Ludwig, T. (2011). Implications of the serpentine phase transition on the behaviour of beryllium and lithium-boron of subducted ultramafic rocks. *Geochimica et Cosmochimica Acta*, *75*(5), 1249–1271. https://doi.org/10.1016/j.gca.2010.12.007

Wenk, H. R. (1973). The structure of the Bergell Alps. *Eclogae Geologicae Helvetiae*, *66*(2), 255–291.

Weyer, S., & Ionov, D. A. (2007). Partial melting and melt percolation in the mantle: The message from Fe isotopes. *Earth and Planetary Science Letters*, *259*(1–2), 119–133. https://doi.org/10.1016/j.epsl.2007.04.033

Wicks, F., & Whittaker, E. (1977). Serpentine textures and serpentinization. *The Canadian Mineralogist*, *15*(4), 459–488.

Williams, H. M., & Bizimis, M. (2014). Iron isotope tracing of mantle heterogeneity within the source regions of oceanic basalts. *Earth and Planetary Science Letters*, *404*, 396–407. https://doi.org/10.1016/j.epsl.2014.07.033

Wilson, A. (1960). The micro-determination of ferrous iron in silicate minerals by a volumetric and a colorimetric method. *Analyst*, *85*(1016), 823–827. https://doi.org/10.1039/an9608500823

SUPPORTING INFORMATION

Additional supporting information can be found online in the Supporting Information section at the end of this article.

FIGURE S1: (a-b) examples of talc (Tlc-a) pseudomorphic after anthophyllite in Talc + olivine metaperidotite containing no Ca (PR-03 and PR-01). c) False colour BSE image showing the distinction between oriented talc matrix. Prograde antigorite (Atg) inclusions and retrograde lizardite (Lz) forming late veins crosscutting olivine porphyroblast. Corresponding RAMAN spectra for serpentine are reported (Azo-17). d) BSE photo micrograph of chlorite (Chl) + olivine (ol) + tremolite (Tr) meta-peridotite containing prismatic enstatite (En). Corresponding EDS spectra are provided (PR-16).

FIGURE S2: Examples of BSE impages where large Cr-rich magnetites (Mag) aggregates as an alteration result of Cr-spinel can still be recognized throughout the contact aureole. Isolated magnetite crystals droplets can also be recognized in antigorite (Atg) serpentinite (a) and in talc (Tlc) + olivine (Ol) + tremolite (Tr) + chlorite (Chl) fels (b to d). Those magnetite are the result of serpentinization reaction then antigorite breakdown. Examples of pentlandite (Pen) + magnetite association in serpentinite (e) and in olivine + enstatite fels (f).

FIGURE S3: Ca-Si-(Mg + Fe^{2+}) ternary diagram for serpentinites and meta-peridotites within the Bergell contact aureole. Data from Trommsdorff and Evans (1972) and Müntener et al. (2010) are also reported as comparison. Symbol distinction was made on the basis of sample locality. Compositions for both serpentinite (serp.) and metaperidotite (M.P.) stand within the tremolite (tr)-olivine (ol)-enstatite (en) triangle. di: diopside. Tlc: talc.

FIGURE S4: (a and b) Representation of the loss of ignition (L.O.I.) of serpentinites and olivine fels found within the Malenco contact aureole as a fonction of the distance with the tonalite intrusion contact. c) Major element composition of serpentinites and olivine fels (in oxide wt. %) and total Fe cation as a function of L.O.I.

FIGURE S5: Binary diagrams showing: a) MnO versus NiO concentration. b) TiO2 versus Al_2O_3 concentration. c) Al_2O_3/SiO_2 ratios versus Yb concentration. and d) (Eu/Eu*) ratio versus Yb. (Eu/Eu* = Eu/([Sm + Gd]/2))) demonstrating the consistency of trace element composition in each ultramafic rock groups defined in the Malenco contact aureole. Symbol distinction was made based on major element geochemistry as defined in Figure 4. Data for mid-ocean-ridge (MOR) and abyssal serpentinites (Kodolányi et al. 2012) and data from partially serpentinized peridotites (Müntener et al. 2010) and metaperidotites from Trommsdorf and Evans (1972) are shown as a comparison.

TABLE S1: Localities. coordinates and overview of key observations.

TABLE S2: Index mineral modes of representative ultramafic rocks studied calculated by least-squares regression (Modfit written by L.- P. Baumgartner). It is considered that all ferric iron goes in magnetite and all aluminium goes in chlorite. Which means that magnetite and chlorite mode are maximum proportion while serpentinite mode is a minimum.

TABLE S3: Mineral composition (in oxide wt.%) for index minerals in selected serpentinites and Olivine + talc fels samples collected within the Malenco contact aureole. Ol: olivine. Serp: serpentine. Tlc: talc. Tr:

tremolite. Cpx: climopyroxene. Chl: chlorite. S.D. Standard deviation.

TABLE S4: *Mg for selected serpentinites and olivine-talc fels and Mg for corresponding index minerals.*

TABLE S5: Oxide composition (in wt.%) for magnetite in selected serpentinites and Olivine + talc fels samples collected within the Malenco contact aureole.

TABLE S6: Elemental composition (in wt.%) for pentlandite in one serpentinite and selected Olivine fels within the Malenco contact aureole

TABLE S7: Bulk rock major element (anhydrous) concentrations obtain by X-ray fluorescence on Li-tetraborate glasses and loss of ignition after samples calcination at ISTE Lausanne. When not analysed (na) by wet chemistry and colorimetry all iron is considered as Fe^{3+}. Trace element concentrations were measured at ISTE lausanne on pieces of Li-tetraborate glasses using a quadrupole spectrometer Agilent 7,700 coupled to a GeoLas 200 M ArF excimer ablation system using NIST SRM612 standard. Bulk Fe isotope were determined using Neptune Plus Multi-Collector Mass Spectrometer at the Laboratoire Magmas et Volcans (LMV) Saint-Etienne.

Table A7: Analyses on NIST standards (30 analyses)

How to cite this article: Lafay, R., Baumgartner, L. P., & Delacour, A. (2023). Preservation of mantle heterogeneities and serpentinization signature during antigorite dehydration: The example of the Bergell contact aureole. *Journal of Metamorphic Geology*, *41*(3), 377–399. https://doi.org/10.1111/jmg.12699